Shell chemistry of the Boreal Campanian bivalve *Rastellum diluvianum* (Linnaeus, 1767) reveals temperature seasonality, growth rates and life cycle of an extinct Cretaceous oyster.

Niels J. de Winter[1]*, Clemens V. Ullmann[2], Anne M. Sørensen[3], Nicolas Thibault[4], Steven Goderis[1], Stijn J.M. Van Malderen[5], Christophe Snoeck[1,6], Stijn Goolaerts[7], Frank Vanhaecke[5], Philippe Claeys[1]

[1]AMGC research group, Vrije Universiteit Brussel, Pleinlaan 2, B-1050 Brussels, Belgium.

[2]Camborne School of Mines, University of Exeter, Penryn, Cornwall, TR10 9FE, UK.

[3]Trap Danmark, Agem All 13, DK-2970, Hørsholm, Denmark.

[4] Department of Geoscience and Natural Resource Management, University of Copenhagen, Øster Voldgade 10, DK-1350 Copenhagen C., Denmark.

[5]A&MS research unit, Ghent University Campus Sterre, Krijgslaan 281, Building S12, B-9000 Ghent, Belgium.

[6]G-Time laboratory, Université Libre de Bruxelles, 50 Avenue F.D. Roosevelt, B-1050, Brussels, Belgium.

[7]Directorate of Earth and History of Life, Royal Belgian Institute of Natural Sciences, Vautierstraat 29, B-1000 Brussels, Belgium.

*Now at: Department of Earth Sciences, Faculty of Geosciences, Utrecht University, the Netherlands

Correspondence to: Niels J. de Winter (niels.de.winter@vub.be)

Abstract

The Campanian age (Late Cretaceous) is characterized by a warm greenhouse climate with limited land ice volume. This makes this period an ideal target for studying climate dynamics during greenhouse periods, which are essential for predictions of future climate change due to anthropogenic greenhouse gas emissions. Well-preserved fossil shells from the Campanian (±78 Ma) high mid-latitude (50°N) coastal faunas of the Kristianstad Basin (southern Sweden) offer a unique snapshot of short-term climate and environmental variability, which complements existing long-term climate reconstructions. In this study, we apply a combination of high-resolution spatially resolved trace element analyses (µXRF and LA-ICP-MS), stable isotope analyses (IRMS) and growth modelling to study short-term (seasonal) variations recorded in the oyster species *Rastellum diluvianum* from the Ivö Klack locality. Geochemical records through 12 specimens shed light on the influence of specimen-specific and ontogenetic effects on the expression of seasonal variations in shell chemistry and allow disentangling vital effects from environmental influences in an effort to refine palaeoseasonality reconstructions of Late Cretaceous greenhouse climates. Growth models based on stable oxygen isotope records yield information on the mode of life, circadian rhythm and reproductive cycle of these extinct oysters. This multi-proxy study reveals that mean annual temperatures in the Campanian higher mid-latitudes were 17 to 19°C with winter minima of ~13°C and summer maxima of 26°C, assuming a Late Cretaceous seawater oxygen isotope composition of -1‰VSMOW. These results yield smaller latitudinal differences in temperature seasonality in the Campanian compared to today. Latitudinal temperature gradients were similar to the present, contrasting with previous notions of "equable climate" during the Late Cretaceous. Our results also demonstrate that species-specific differences and uncertainties in the composition of Late Cretaceous seawater prevent trace element proxies (Mg/Ca, Sr/Ca, Mg/Li and Sr/Li) to be used as reliable temperature proxies for fossil oyster shells. However, trace element profiles can serve as a quick tool for diagenesis screening and investigating seasonal growth patterns in ancient shells.

1. Introduction

49   The Late Cretaceous was marked by a long cooling trend that brought global mean annual temperatures

50   (MAT) down from the mid-Cretaceous climate maximum (±28°C surface ocean temperatures) in the

51   Cenomanian and Turonian (±95 Ma) to slightly cooler temperatures (±22°C surface ocean temperatures)

52   around the Campanian-Maastrichtian boundary (±72.1 Ma; Clarke and Jenkyns, 1999; Pearson et al., 2001;

53   Huber et al., 2002; Friedrich et al., 2012; Scotese, 2016). This cooling trend was likely caused by a change

54   in ocean circulation, initiated by the opening of the Equatorial Atlantic Gateway that separated the proto-

55   North and -South Atlantic Ocean basins (Friedrich et al., 2009). The cooling trend is well documented in

56   stable oxygen isotope records from the white chalk successions of the Chalk Sea, which covered large

57   portions of northwestern Europe during the Late Cretaceous Period (Reid, 1973; Jenkyns et al., 1994; Jarvis

58   et al., 2002; Voigt et al., 2010). The connection of the Chalk Sea to the (proto-)North Atlantic Ocean makes

59   it an interesting area of study to constrain Late Cretaceous paleogeography and climate. These chalk

60   successions featured in various paleoclimate studies, because they are accessible in good outcrops and

61   consist predominantly of calcareous nannofossils which were thought to faithfully record sea surface

62   conditions (e.g. Jenkyns et al., 1994). However, recent studies (e.g. O'Brien et al., 2017; Tagliavento et al.,

63   2019) have shown that diagenetic overprinting likely biases these records towards cooler temperatures,

64   resulting in the apparent Cool Tropics Paradox (Pearson et al., 2001). Even though sea level changes seem

65   to indicate possible small changes in land ice volume during the Late Cretaceous, warm high-latitude

66   paleotemperatures likely rule out the possibility of extensive polar ice sheets comparable in volume to

67   modern ice caps (Barrera and Johnson, 1999; Huber et al., 2002; Jenkyns et al., 2004; Miller et al., 2005;

68   Thibault et al., 2016).

69   Given its warm, essentially land-ice free conditions, the Campanian serves as an interesting analogue for

70   Earth's climate in the future, should anthropogenic and natural emissions continue to contribute to the rise

71   in global temperatures and decrease global ice volume on Earth (IPCC, 2013; Donnadieu et al., 2016).

72   However, most Late Cretaceous climate reconstructions focus on reconstructing and modelling long-term

73   evolutions of humid/arid conditions on land or past atmospheric and oceanic temperatures (DeConto et al.,

74   1999; Thibault et al., 2016; Yang et al., 2018). Data on the extent of seasonal variability from this time

75   period, especially outside the tropics, are scarce, although seasonality constitutes a fundamental

76   component of the climate system (Steuber, 1999; Steuber et al., 2005; Burgener et al., 2018). Furthermore,

3

77 many proxies used for paleoclimate reconstruction risk seasonal bias, and thus independent seasonality

78 reconstructions serve as important tools to verify other climate reconstructions.

79

80 **2. Background**

81 **2.1 Geological setting**

82 The Kristianstad Basin, our study site, is located on the southeastern Baltic Sea coast of the southern

83 Swedish province of Skåne, which is presently located at 56°2' N, 14° 9' E (see **Fig. 1**), somewhat higher

84 than its Campanian paleolatitude, which is estimated at 50°N (van Hinsbergen et al., 2015). The uppermost

85 lower Campanian shallow marine sediments deposited at Ivö Klack consist of sandy and silty nearshore

86 deposits containing carbonate gravel (Christensen, 1975; 1984; Surlyk and Sørensen, 2010; Sørensen et

87 al., 2015). The depositional setting is described as a rocky coastline that was inundated during the

88 maximum extent of the Late Cretaceous transgression (Kominz et al., 2008; Csiki-Sava et al., 2015). Since

89 the region has remained tectonically quiet since the Campanian, the deposits of Kristianstad Basin localities

90 remain at roughly the same altitude as when they were deposited and have been subject to limited burial

91 (Christensen, 1984; Surlyk and Sørensen, 2010).

92 The rocky shore deposits of Ivö Klack are characterized by a diverse shelly fauna, consisting of well-

93 preserved fossils and fragments of brachiopods, belemnites, echinoids and asteroids, polychaete worms,

94 gastropods, corals, ammonites and thick-shelled oysters, with a total of almost 200 different recognized

95 species (Surlyk and Sørensen, 2010). In this diverse rocky shore ecosystem, various habitat zones can be

96 distinguished, each with their distinct suite of organisms adapted to local conditions of varying amounts of

97 sunlight, sedimentation and turbulence (Surlyk and Christensen, 1974; Sørensen et al., 2012). This unique

98 combination of marine biodiversity and preservation of original calcite shell material makes the localities in

99 the Kristianstad Basin ideal for studying sub-annual variability in shell chemistry and reconstructing

100 paleoseasonality and environmental change in the Campanian (Sørensen et al., 2015).

101 **2.2 Bivalve shells**

4

102 Fossil bivalve shells offer a valuable archive for studying past climates on a seasonal scale. Incremental

103 measurements of shell chemistry in growth direction (sclerochronology studies) potentially yield records of

104 seasonal changes in the environment (Mook, 1971; Jones, 1983; Klein et al., 1996; Schöne and Gillikin,

105 2013). Their distribution allows paleoseasonality reconstructions from bivalves across a wide range of

106 latitudes (Roy et al., 2000; Jablonski et al., 2017), and the preservation potential of calcitic shell structures

107 (especially in oyster shells) makes them ideal, if not unique, recorders of pre-Quarternary seasonality and

108 sub-annual environmental change (Brand and Veizer, 1980; 1981; Al-Aasm and Veizer, 1986a; b;

109 Immenhauser et al., 2005; Alberti et al., 2017). The incremental deposition of shell carbonate means, in

110 theory, that the limits in terms of time resolution of the bivalve shell archive are governed by sampling

111 resolution rather than the resolution of the record itself. While periods of growth cessation can occur

112 (especially in high latitudes, Ullmann et al., 2010) and the true mechanisms of shell deposition on a very

113 high (e.g. daily) temporal resolution are poorly constrained (see de Winter et al., 2020a and references

114 therein), in practice incremental shell deposition allows reconstructions of changes down to sub-daily

115 timescales given the right sampling techniques (Schöne et al., 2005; Sano et al., 2012; Warter et al., 2018;

116 de Winter et al., 2020a). Examples of chemical proxies used in such sclerochronology studies include stable

117 carbon and oxygen isotope ratios and trace element ratios (e.g. Steuber et al., 2005; Gillikin et al., 2006;

118 McConnaughey and Gillikin, 2008; Schöne et al., 2011; de Winter et al., 2017a; 2018).

119 **2.3 Trace element proxies**

120 The incorporation of trace elements and carbon isotopes into bivalve shells is influenced by so-called vital

121 effects: biological controls on the incorporation of elements in the shell independent of the environment

122 (Weiner and Dove, 2003; Gillikin et al., 2005). These vital effects have been shown to mask the

123 characteristic relationships between shell trace element chemistry and the environment and appear to be

124 distinct not only between different bivalve species but also between specimens of different ontogenetic age

125 (Freitas et al., 2008). Differences between bivalve families mean that the trace element chemistry of some

126 taxa (like scallops: Family Pectinidae) are especially affected by vital effects (Lorrain et al., 2005; Freitas

127 et al., 2008), while other families like oysters (Family Ostreidae) seem to be more robust recorders of

128 environmental conditions (Surge et al., 2001; Surge and Lohmann, 2008; Ullmann et al., 2010; 2013). The

129 effect on shell composition and preservation of changes in microstructure and the amount of organic matrix

130   present in different shell layers introduces uncertainty as to which parts of the shells are well-suited for

131   reconstruction purposes (Carriker et al., 1991; Kawaguchi et al., 1993; Dalbeck et al., 2006; Schöne et al.,

132   2010; 2013). The key to disentangling vital effects from recorded environmental changes lies in the

133   application of multiple proxies and techniques on the same bivalve shells (the "multi-proxy approach"; e.g.

134   Ullmann et al., 2013; de Winter et al., 2017a; 2018) and to base reconstructions on more than one shell

135   (Ivany, 2012).

136   **2.4 Stable isotope ratios**

137   Because nearly all bivalves precipitate their shells at or near oxygen isotope equilibrium, the stable oxygen

138   isotope ratio of bivalve shell carbonate is less susceptible to vital effects, such as growth kinetics (Uchikawa

139   and Zeebe, 2012). Therefore, stable oxygen isotope ratios in bivalve shell carbonate ($\delta^{18}O_c$) are solely

140   dependent on calcification temperature and sea water oxygen isotope composition ($\delta^{18}O_{sw}$), and this proxy

141   is frequently used in sclerochronology studies as a paleothermometer (Kim and O'Neil, 1997; Schöne et

142   al., 2005; Butler et al., 2013; Ullmann et al., 2013; Huyghe et al., 2015; de Winter et al., 2020b). Oxygen

143   isotope records can function as a reference in the above-mentioned multi-proxy studies aimed at resolving

144   vital effects, environmental and climatic changes. However, the weakness of this proxy lies in the fact that

145    $\delta^{18}O_{sw}$ is not always known, especially in deep time settings (Veizer and Prokoph, 2015). As a result, a

146   constant $\delta^{18}O_{sw}$ of 0‰VSMOW for modern icehouse climate conditions, or -1‰VSMOW for an ice-free

147   world (such as the Eocene or the Late Cretaceous; after Shackleton, 1986) is often assumed (e.g.

148   Andreasson and Schmitz, 1996; Ivany and Runnegar, 2010; Huyghe et al., 2015). An offset of 1‰ between

149   assumed $\delta^{18}O_{sw}$ and actual $\delta^{18}O_{sw}$ can result in a ~4.6°C temperature offset in temperature reconstructions

150   (Kim and O'Neil, 1997) This assumption may therefore introduce inaccuracies in absolute temperature

151   reconstructions, but relative variations in $\delta^{18}O_c$ can still yield important insights into high-resolution climate

152   dynamics.

153   In marine mollusks, dissolved inorganic carbon (DIC) in the ambient sea water contributes the largest

154   fraction of carbon (90%) used for shell mineralization (McConnaughey, 2003; Gillikin et al., 2007) and

155   therefore heavily influences $\delta^{13}C$ values of shell carbonate. However, changes in respiration rates can alter

156   the carbon budget of shell carbonate by adding or removing isotopically light respired carbon in the form of

157   CO_2 (Lorrain et al., 2004). Environmental changes in DIC can also have a strong influence on this carbon

158   budget, especially when bivalves grow in nearshore or estuarine conditions with large (seasonal) variations

159   in environmental $\delta^{13}C$ of DIC and organic carbon (Gillikin et al., 2006). Conceptual models exist that attempt

160   to correlate shell $\delta^{13}C$ in modern mollusks to environmental and physiological variations, but these require

161   knowledge of ambient CO_2 pressures and $\delta^{13}C$ values of DIC, gas ventilation rates in the animal and CO_2

162   and O_2 permeabilities of calcifying membranes (McConnaughey et al., 1997), which are not available in

163   fossil bivalve studies.

164   **2.5 Aim**

165   In this study, we present a detailed, multi-proxy comparison of the growth and chemistry of well-preserved

166   fossil shells of the thick-shelled oyster *Rastellum diluvianum* (Linnaeus, 1767) recovered from the Ivö Klack

167   locality on the northern edge of the Kristianstad Basin. We combine stable isotope proxies conventional in

168   sclerochronological studies ($\delta^{13}C$ and $\delta^{18}O$; e.g. Goodwin et al., 2001; Steuber et al., 2005) with less well-

169   established trace element proxies (Mg/Ca, Sr/Ca, Mg/Li and Sr/Li; e.g. Bryan and Marchitto, 2008; Schöne

170   et al., 2011; Füllenbach et al., 2015; Dellinger et al., 2018) and growth modelling based on $\delta^{18}O$ seasonality

171   (Judd et al., 2018) in an attempt to disentangle the effects of growth rate, reproductive cycle and

172   environmental change on shell chemistry. The data gathered in this study allow a detailed discussion on

173   seasonal changes in temperature and water chemistry in the coastal waters of the Kristianstad Basin in the

174   late early Campanian, as well as on the life cycle of *R. diluvianum* and its response to seasonal changes in
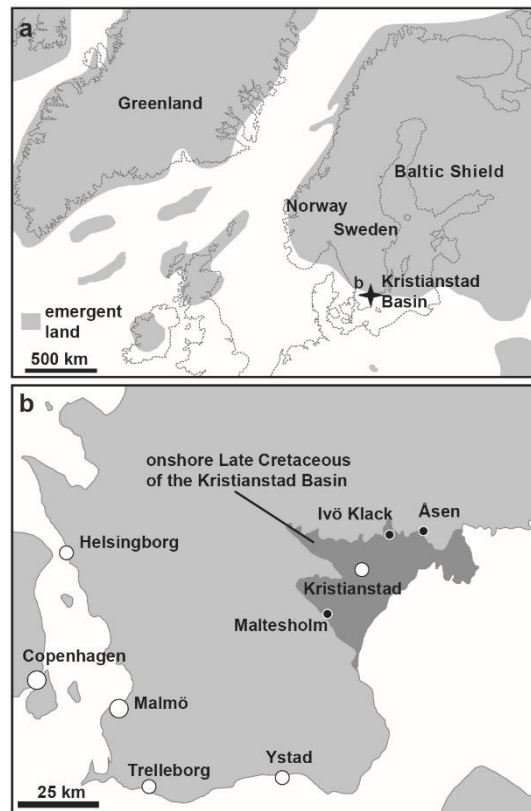
175   its environment.

176

Figure 1: Paleogeographic map of the Boreal Chalk Sea (**a**) and the area of present-day southern Sweden (**b**) showing the location of Ivö klack (modified after Sørensen et al., 2015)
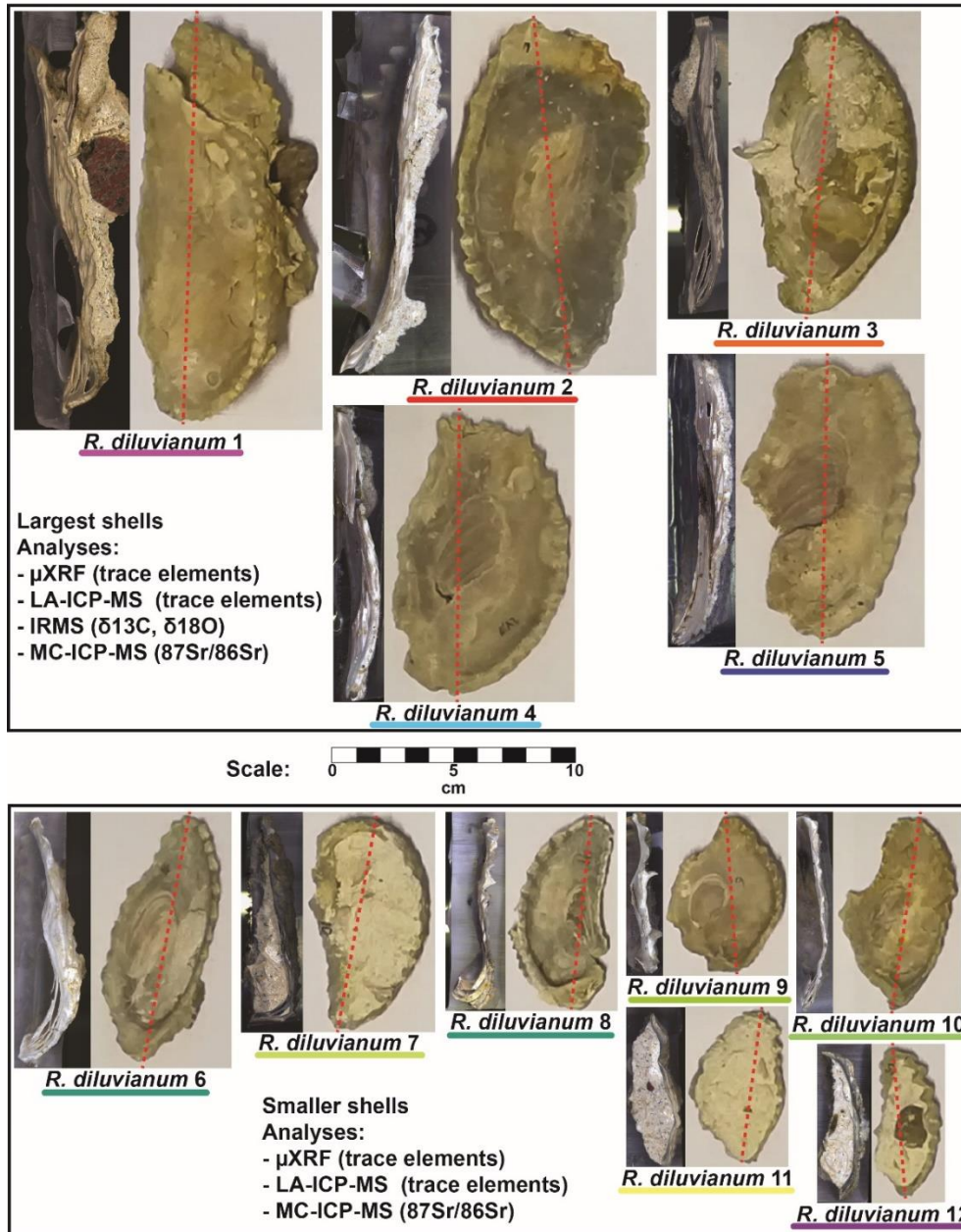
3. Materials and Methods

3.1 Sample acquisition and preparation

Complete valves of twelve individual *R. diluvianum* oysters were obtained from the Ivö Klack locality (see **Fig. 2**). Specimens of *R. diluvianum* were found *in situ* attached to the vertical sides of large boulders that characterized the rocky shore of Ivö Klack (Surlyk and Christensen, 1974) and are biostratigraphically assigned to the latest early Campanian *B. mammillatus* belemnite zone. The valves were cleaned and fully embedded in Araldite® 2020 epoxy resin (Bodo Möller Chemie Benelux, Antwerp, Belgium). Dorsoventral slabs (±10 mm thick) were cut perpendicular to the hinge line using a water-cooled slow rotating saw with a diamond-coated blade (thickness ± 1 mm; **Fig. 2**). The surfaces cut on the central growth axis were progressively polished using silicon-carbide polishing disks (up to P2500, or 8.4 µm grain size). Polished surfaces were scanned at high (6400 dpi) resolution using an Epson Perfection 1650 flatbed color scanner (Seiko Epson Corp., Suwa, Japan). Resulting color scans of all polished *R. diluvianum* shell cross sections are provided in **Fig. 2** and **S1**. Shell microstructures in *R. diluvianum* shells were studied in detail on high-resolution scans and by using reflected light optical microscopy. Microstructural features were used to reconstruct the relative timing of shell growth (see **Fig. 3**). Fragments of visually well-preserved material from different microstructures in the shells were coated with gold and studied under a Scanning Electron Microscope (Quanta 200 ESEM) and imaged at 1000x – 2000x magnification (**Fig. 3b-e**). Chemical analyses were carried out sequentially on polished cross sections in order of destructive character of sampling (starting with the least destructive measurements: µXRF, LA-ICP-MS, microdrilling for IRMS and finally MC-ICP-MS analysis on ~26 mg samples).

Overview of *Rastellum diluvianum* shells

R. diluvianum 1

R. diluvianum 2

R. diluvianum 3

R. diluvianum 4

R. diluvianum 5

Largest shells
Analyses:
- µXRF (trace elements)
- LA-ICP-MS (trace elements)
- IRMS (δ13C, δ18O)
- MC-ICP-MS (87Sr/86Sr)

Scale: 0 5 10 cm

R. diluvianum 6

R. diluvianum 7

R. diluvianum 8

R. diluvianum 9

R. diluvianum 10

R. diluvianum 11

R. diluvianum 12

Smaller shells
Analyses:
- µXRF (trace elements)
- LA-ICP-MS (trace elements)
- MC-ICP-MS (87Sr/86Sr)

Figure 2: Overview of the 12 *Rastellum diluvianum* shells used in this study. All shells are depicted at the same scale (see scalebar in center of image). Colors of the lines under sample names correspond to the colors of the lines in **Fig. 4**, **Fig. 6**, **Fig. 8** and **Fig. 10**. Every shell is represented by an image of the inside of the valve analyzed, as well as a color scan of the cross section through the shell on which high-resolution analyses were carried out. Dashed red lines show the location of these cross sections. The largest 5 shells (1-5, on top half) were sampled for IRMS analyses (δ^{13}C and δ^{18}O). All shells were subjected to micro X-ray fluorescence (µXRF), laser ablation inductively coupled plasma mass spectrometry (LA-ICP-MS) and multi-cup inductively coupled plasma mass spectrometry (MC-ICP-MS) analyses. Full-size versions of the high-resolution color scans of shell cross sections are provided in **S1**.
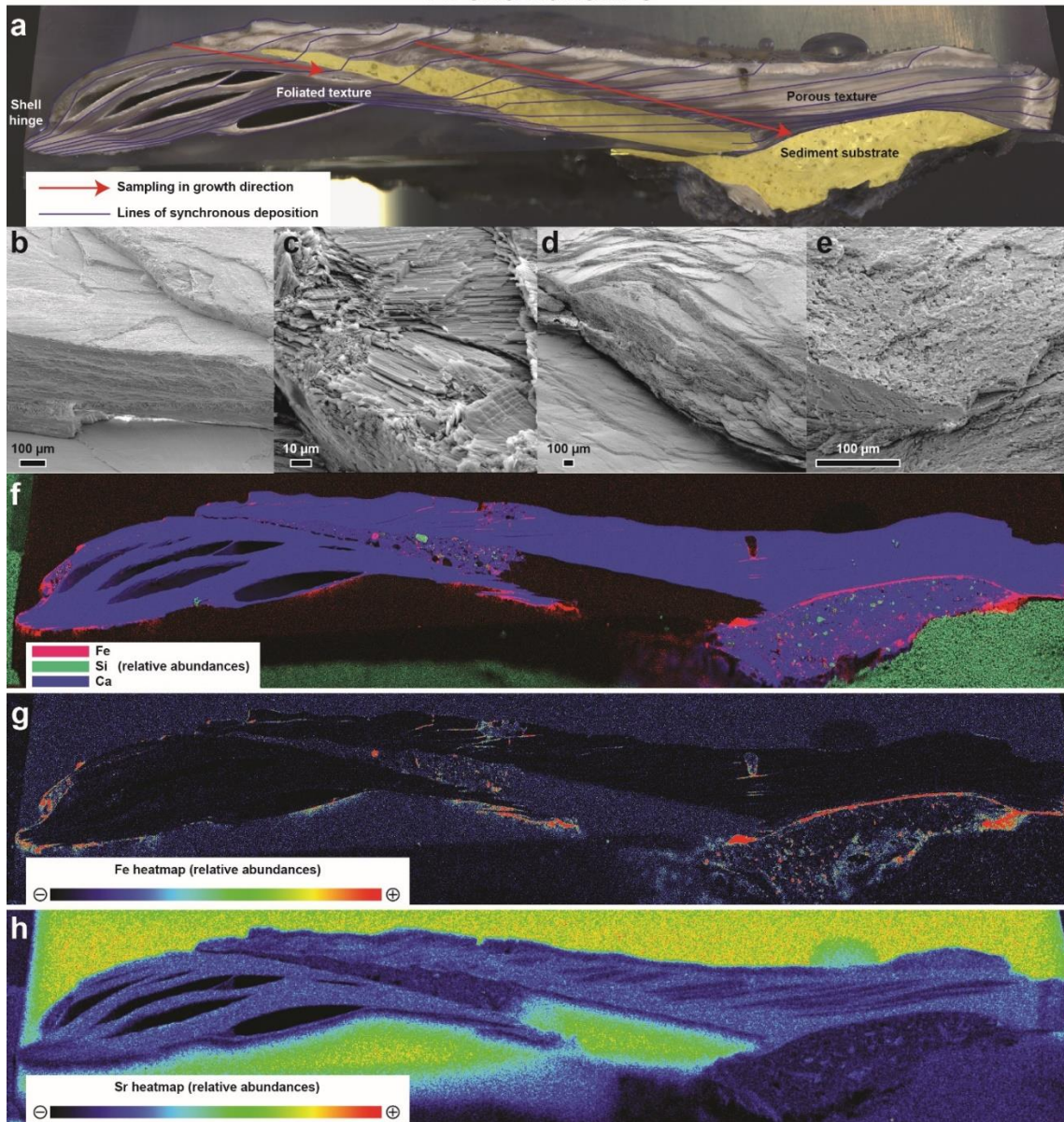
Figure 3: Overview image showing a high-resolution color scan of the cross section through *R. diluvianum* 3 (**a**) on which the different shell textures as well as the directions of high-resolution analyses (in growth direction) are indicated. Thin blue lines denote parts of the shell that were deposited at the same time (growth increments). Areas marked in yellow represent sediment infilling below and within the valves. (**b**) and (**c**) show SEM images of the well-preserved foliated calcite in the shell. More porous structures in the shell (vesicular calcite) are depicted in SEM images shown in (**d**) and (**e**). Below are shown three XRF elemental maps of the same cross section: An RGB-colored map displaying the relative abundances of Fe, Si and Ca (**f**), A heatmap of Fe concentrations (**g**; see scalebar below map) and a heatmap of Sr concentrations (**h**; see scalebar below map). XRF mapping only yields relative (semi-quantitative) abundance of elements.

3.2 Micro-XRF mapping

Elemental abundance maps of all *R. diluvianum* shell cross sections were obtained using a Bruker Tornado M4 energy-dispersive micro-X-Ray Fluorescence scanner (µXRF; Bruker nano GmbH, Berlin, Germany). All µXRF analyses carried out with the Bruker M4 Tornado are non-destructive. The µXRF is equipped with a Rh filament metal-ceramic tube X-Ray source operated at 50 kV and 600 µA (30 W; maximum energy settings). The circular spot projected on the same surface is estimated to have a diameter of 25 µm (Mo-Kα). A µm-precision XYZ translation stage allows for quick and precise sample movement such that a grid of 25 µm XRF spots can be measured on the sample surface by continuous scanning to construct elemental maps ($3 * 10^6$ - $5 * 10^6$ pixels per map). Exposure times of the X-ray beam per sampling position in mapping mode (1 ms/pixel) are too short to gain adequate signal-to-noise ratio for pixel-by-pixel quantification of elemental concentrations. Instead, processing of entire map surfaces using the Bruker Esprit™ software allows semi-quantitative elemental abundance maps to be created of the sample surface based on a mapping of the count rate in 'Regions of Interest' of elements (see de Winter and Claeys, 2016; de Winter et al., 2017b; **Fig. 3**). XRF maps allow for a rapid assessment of the preservation state of original shell calcite based on variations in Si, Mn, Fe and Sr concentrations and guide the formulation of sampling protocols for further analyses (de Winter and Claeys, 2016; **Fig. 3**). Results of XRF mapping on all 12 *R. diluvianum* shell cross sections are provided in **S2**.

3.3 Micro-XRF line scans

After XRF mapping, quantitative line scans were measured in growth direction on shell cross sections. Dwell times of 60 seconds per measurement yielded sufficiently high signal-to-noise ratios for individual points in line scans to be quantified. This acquisition time was chosen so as to provide the optimal compromise between increasing run time (improved signal/noise ratio; enhanced reproducibility) and increasing the number of sampling positions (improving sampling density and allowing duplicate measurements) for the elements Mg, Al, Si, P, S, Ca, Ti, Mn, Fe, Cu, Zn and Sr (see discussion in de Winter et al., 2017b). The sampling interval of line scans was 50 µm, adding up to a total of 11056 individual quantitative XRF spectra measured for this study. Spectra were quantified using the Bruker Esprit software calibrated using the matrix-matched BAS-CRM393 limestone standard (Bureau of Analyzed samples,

245   Middlesbrough, UK), after which individual measurements were calibrated offline using 7 matrix-matched

246   certified reference materials (CCH1, COQ1, CRM393, CRM512, CRM513, ECRM782 and SRM1d), which

247   were treated as samples (see Vansteenberge et al., 2020). R^2 values of calibration curves exceeded 0.99

248   and reproducibility standard deviations were better than 10% relative to the mean. Even though line scans

249   were positioned on well-preserved shell calcite based on the XRF map results, a second check was carried

250   out in which individual points were rejected based on conservative thresholds for diagenetic recrystallization

251   or detrital contamination ([Ca] < 38 wt%, [Si] > 1 wt%, [Mn] > 200 µg/g or [Fe] > 250 µg/g; [Sr]/[Mn] < 100

252   mol/mol; see Al-Aasm and Veizer, 1986a; Sørensen et al., 2015). Concentrations of Ca, Mg and Sr in well-

253   preserved shell sections were used to explore the potential of Mg/Ca and Sr/Ca molar ratios as

254   paleoenvironmental proxies. Unprocessed results of XRF line scanning are provided in **S3**.

255   **3.4 LA-ICP-MS line scans**

256   Spatially resolved elemental concentrations for Li, B, Mg, Si, P, Ca, Ti, V, Cr, Mn, Fe, Ni, Zn, Rb, Sr, Ba,

257   Pb and U were calculated from a calibrated transient MS signal recorded during Laser Ablation-Inductively

258   Coupled Plasma-Mass Spectrometry (LA-ICP-MS) line scanning in the growth direction (parallel to the XRF

259   line scans) on shell cross sections. LA-ICP-MS measurements were carried out at the Atomic and Mass

260   Spectrometry – A&MS research unit of Ghent University (Ghent, Belgium) using a 193 nm ArF*excimer-

261   based Analyte G2 laser ablation system (Teledyne Photon Machines, Bozeman, USA), equipped with a

262   HelEx 2 double-volume ablation cell, coupled to an Agilent 7900 quadrupole-based ICP-MS unit (Agilent,

263   Tokyo, Japan). Continuous scanning along shell transects using a laser spot with a diameter of 25 µm,

264   scan speed of 50 µm/s and detector mass sweep time of 0.5 s yielded profiles with a lateral sampling

265   interval of 25 µm, amounting to a total of 9505 LA-ICP-MS data points gathered. The aerosol was

266   transported using He carrier gas into the ICP-MS unit via the aerosol rapid introduction system (ARIS;

267   Teledyne Photon Machines, Bozeman, USA). Elemental concentrations were calibrated using bracketed

268   analysis runs on US Geological Survey (USGS) BCR-2G, BHVO-2G, BIR-1G, GSD-1G and GSE-1G and

269   National Institute of Standards and Technology (NIST) SRM612 and SRM610 certified reference materials.

270   Calcium concentrations (measured via ^{43}Ca) were used as internal standard for data normalization and drift

271   correction during the measurement campaign, and Ca concentrations of 38.5 wt% were assumed for

272   pristine shell carbonate. Coefficients of determination (R^2) of a linear model fitted to the calibration curves

273 were better than 0.99 and the standard deviation of reproducibility for elemental concentrations was better

274 than 5% relative to the mean value. Individual LA-ICP-MS measurements were inspected for diagenetic

275 alteration or contamination by detrital material using the same thresholds as used for XRF data (see above).

276 LA-ICP-MS and µXRF measurements were combined to cover a wider range of elements, since some

277 elements (e.g. S and Sr) were measured more reliably using µXRF, while others (e.g. Li or Ba) could only

278 be quantified using LA-ICP-MS. Concentrations of Li, Mg, and Sr were used to explore the potential of

279 Mg/Li and Sr/Li molar ratios as proxies for paleoenvironmental change. Unprocessed results of LA-ICP-MS

280 line scans are provided in **S4**.

281 **3.5 Isotope Ratio Mass Spectrometry**

282 A transect of powdered samples (±200 µg) was extracted for Isotope Ratio Mass Spectrometry (IRMS)

283 analysis in growth direction along well-preserved foliated calcite (**Fig. 3**) in the five largest of the twelve *R.*

284 *diluvianum* shells (*R. diluvianum* 1-5; see **Fig. 2**) using a microdrill (Merchantek/Electro Scientific Industries

285 Inc., Portland (OR), USA) equipped with a 300 µm diameter tungsten carbide drill bit, coupled to a

286 microscope (Leica GZ6, Leica Microsystems GmbH, Wetzlar, Germany). A total of 531 IRMS samples were

287 taken at an interspacing of 250 µm. Stable carbon and oxygen isotope ratios ($\delta^{13}C$ and $\delta^{18}O$) were

288 measured in a NuPerspective IRMS equipped with a NuCarb carbonate preparation device (Nu

289 Instruments, UK). The sample size (50-100 µg) allowed duplicate measurements to be carried out regularly

290 (roughly once every 30 samples) to assess reproducibility. Samples were digested in 104% phosphoric

291 acid at a constant temperature of 70°C and the resulting CO_2 gas was cryogenically purified before being

292 led into the IRMS through a dual inlet system. Isotope ratios were corrected for instrumental drift and

293 fractionation due to variations in sample size and the resulting values are reported relative to the Vienna

294 Pee Dee Belemnite standard (‰VPDB) using repeated measurements of the IA-603 stable isotope

295 standard (International Atomic Energy Agency, Vienna, Austria). Reproducibility of $\delta^{18}O$ and $\delta^{13}C$

296 measurements on this standard were better than 0.1‰ and 0.05‰ (1σ; N=125) respectively. All stable

297 isotope analysis results are provided in **S5** and plots of stable isotope and trace element records from all

298 shells are given in **S6**.

299 **3.6 Growth and age modelling**

300   Stable oxygen isotope curves measured in *R. diluvianum* were used to produce age models for the growth

301   of the shell using a bivalve growth model written in MatLab (Mathworks, Natick, MA, USA) which simulates

302    $\delta^{18}O$ curves using a combination of growth and temperature sinusoids (Judd et al., 2018). This simulation

303   model was modified to calculate its temperatures based on calcite $\delta^{18}O$ (following Kim and O'Neil, 1997)

304   rather than from the aragonite $\delta^{18}O$-temperature relationship used in the original approach (after Grossman

305   and Ku, 1986; see Judd et al., 2018). A value of -1.0‰ VSMOW was assumed for $\delta^{18}O$ of Campanian

306   ocean water (Shackleton, 1986; Thibault et al., 2016). Additional minor modifications in the source code

307   allowed results of intermediate calculation steps in the model to be exported. The modified Matlab source

308   code is provided in **S7**. Note that this model assumes that the shape and absolute value of $\delta^{18}O$ curves

309   depend solely on water temperature and growth rate (ignoring changes in $\delta^{18}O_{sw}$), and that a modelled year

310   contains 365 days by construction (while this number should be slightly larger in the Late Cretaceous; de

311   Winter et al., 2020a). Despite these caveats, shell chronologies reconstructed from seasonal patterns in

312    $\delta^{18}O$ should still be reliable as they are only based on the shape of the $\delta^{18}O$ curves. Uncertainties on

313   modelled temperature curves were derived by propagating the measurement uncertainty on $\delta^{18}O$. Age

314   models thus obtained for shells *R. diluvianum* 1-5 were used to align all proxy records on a common time

315   axis. Age models for *R.diluvianum* 6-12 were constructed by extrapolating relationships between modelled

316   seasonality and microstructures and trace element concentrations observed in *R. diluvianum* 1-5.

317   Simultaneously deposited microstructural features in shell cross sections (see **Fig. 3**) were used to

318   determine the actual dorsoventral height of the shells at different ages, linking shell height to the age and

319   allowing the construction of growth curves for all twelve *R. diluvianum* shells. The total age and the season

320   of spawning (or: the start of shell growth) were determined by extrapolating the $\delta^{18}O$-based age models

321   and by using the relationship between $\delta^{18}O$ profiles and trace element records and growth increments

322   observed in the shell.

323   **3.7 Strontium isotope analysis**

324   Samples (on average 26 mg) for strontium isotope analysis were obtained by drilling the well-preserved

325   foliated calcite in all shells using a Dremel 3000 dental drill with a 0.5 mm tungsten carbide drill bit. Calcite

326   samples were placed in Teflon beakers (Savillex LLC, Eden Prairie, MN, USA), dissolved in subboiled

327 concentrated (14 M) nitric acid (HNO_3) at 120°C and left to dry out at 90°C overnight, after which the residue

328 was redissolved in 2 M HNO_3. Carbonate-bound strontium in the samples was purified following the ion-

329 exchange resin chromatography method detailed in Snoeck et al. (2015). The $^{87}Sr/^{86}Sr$ of purified Sr

330 samples were determined using a Nu Plasma (Nu Instruments Ltd, Wrexham, UK) multi-collector (MC) ICP-

331 MS unit in operation at the Université Libre de Bruxelles (ULB). During the measurement run, repeated

332 analyses of NIST SRM987 standard solution yielded a ratio of 0.710250 ± 0.000040 (2 SD; N = 14),

333 statistically consistent with the literature value of 0.710248 ± 0.000058 (2 s.e.; McArthur et al., 2001; Weis

334 et al., 2006). All results were corrected for instrumental mass discrimination by internal normalization and

335 normalized to the literature value of NIST SRM987 (0.710248) through a standard-sample bracketing

336 method. For each sample, $^{87}Sr/^{86}Sr$ are reported with 2σ uncertainty (**S8**).

337

338
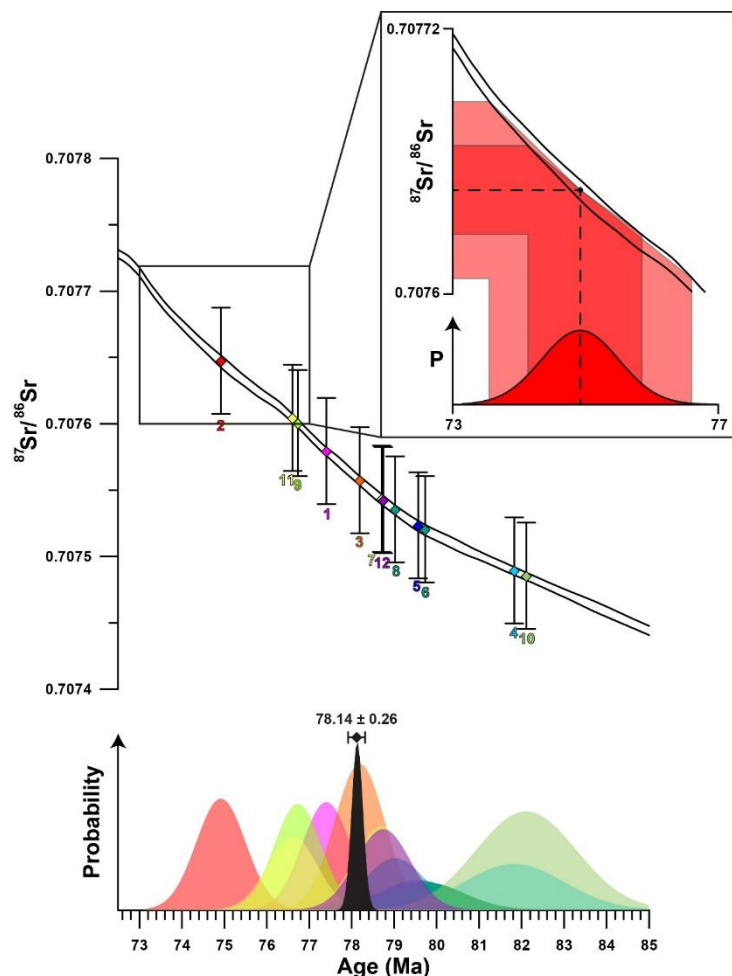
Figure 4: Plot showing the results of Sr-isotopic analyses with error bars (2σ) plotted on the Sr-isotope curve of McArthur et al. (2016; top of image). Numbers below the error bars indicate specimen number. Measurements from the 12 specimens of *R. diluvianum* are represented by parallelograms in different colors which match the probability distributions plotted below. The probability distribution curves in the lower pane show the distribution of uncertainty on each Sr-isotope measurement as well as the uncertainty on the Sr-isotope curve propagated to the age domain (colors of individual shells are the same as in **Fig. 2**). Insert shows schematically how uncertainties of the isotope measurements as well as the isotope curve are propagated into the age domain. The black curve shows the total uncertainty distribution function compiled from the 12 individual measurements following Barlow (2004), with the combined age estimate including uncertainty (2σ) shown above.

348

349

3.8 Strontium isotope dating

351 *R.* diluvianum specimens were independently dated by comparing $^{87}Sr/^{86}Sr$ values measured in the

352 samples with the Sr-isotope curve in the 2016 Geological Timescale (McArthur et al., 2016). Uncertainties

353 in $^{87}Sr/^{86}Sr$ measurements were propagated into dates by finding the closest date of the mean $^{87}Sr/^{86}Sr$

354 value as well as the dates of the minimum (-2σ) and maximum (+2σ) $^{87}Sr/^{86}Sr$ values by linearly interpolating

355 ages in the $^{87}Sr/^{86}Sr$ curve matching the measured $^{87}Sr/^{86}Sr$ value, including the uncertainty estimated on

356 the Sr-isotope curve itself. A composite age for the Ivö Klack deposits was obtained by combining the age

357 uncertainty distributions of the individually dated $^{87}Sr/^{86}Sr$ samples into a single age. Due to the non-linear

358 shape of the $^{87}Sr/^{86}Sr$ curve, uncertainties on the $^{87}Sr/^{86}Sr$ ages were asymmetrical. Since no mathematical

359 solution exists for the combination of asymmetric uncertainties, the asymmetric uncertainty on the total age

360 had to be approximated through maximum likelihood estimation using the combined log likelihood function

361 (Barlow, 2003). The approximation of the total uncertainty of combined $^{87}Sr/^{86}Sr$ dating results in this study

362 was carried out using the mathematical approach of Barlow (2004) in R (R Core Team, 2013; Roger Barlow,

363 personal communication; code available on https://zenodo.org/record/1494909). The uncertainty interval of

364 the composite age is represented by 2 times the standard error (~95.5% confidence level). A plot of the

365 uncertainty distributions of the individual specimens and the total uncertainty distribution is shown in **Fig.**

366 **4**. Raw $^{87}Sr/^{86}Sr$ data are provided in **S8**.

367

4. Results

4.1 Strontium isotope dating

370 Results of strontium isotope analyses are given in **S8**. The mean strontium isotope ratio of all *R. diluvianum*

371 specimens is 0.707552 (±0.000112; 95% confidence level). The compilation of $^{87}Sr/^{86}Sr$ results from 12

372 specimens of *R. diluvianum* (**Fig. 4**) shows how age estimates from individual specimens have considerable

373 uncertainties (standard deviations around 1 Myr, see **S8**), yet the uncertainty on the composite age is

374 significantly smaller. The composite age for the Ivö Klack deposits is 78.14 Ma (±0.26; 95% confidence

375   level). This result places the age of the Ivö Klack deposits close to the early/late Campanian boundary when

376   applying a twofold division of the Campanian and in the middle Campanian when applying a threefold

377   division scheme (Ogg et al., 2016). This age estimate is similar to the age obtained when plotting the *B.*

378   *mammilatus* zone on the recent integration schemes of the Campanian (Wendler, 2013). Earlier estimates

379   (Christensen, 1997; Surlyk and Sørensen, 2010; Sørensen et al., 2015) yielded ages about 2-4 Myr older

380   (80-82 Ma), but those relied on presently outdated and partly incorrect age models.

381   **4.2 Shell structure and preservation**

382   A combination of high-resolution color scans, SEM images and µXRF mapping of shell cross sections

383   reveals that *R. diluvianum* shells consist of thin layers of dark, foliated calcite, interwoven with lighter, more

384   porous carbonate layers (**Fig. 3a-e**). The latter are characterized by higher concentrations of Mn, Fe and

385   Si and lower Sr concentrations (**Fig. 3f-h**). Foliated calcite layers are more densely packed on the inside of

386   the shell, especially in the region of the adductor muscle scar, and at the shell hinge (**Fig. 3a**). They are

387   characterized by high Sr concentrations and low concentrations of Mn, Fe and Si (**Fig. 3f-h**; **S2**). Further

388   away from the shell hinge and the inside of the valve, porous carbonate layers become more dominant. In

389   these regions, µXRF mapping also clearly shows that detrital material (high in Si and Fe) is often found

390   between the shell layers (**Fig. 3f**). SEM images show that the shell structure of *R. diluvianum* strongly

391   resembles that of modern oyster species, as described in previous studies (**Fig. 3b-e**; Carriker et al., 1979;

392   Surge et al., 2001; Ullmann et al., 2010; 2013; Zimmt et al., 2018). The major part of the shell consists of

393   calcite, of which the foliated structures were sampled for chemical analyses in this study. As in modern

394   oyster species, aragonite may originally have been deposited on the resilium of the shell, but this region is

395   not considered for analyses (see outer tip of shell hinge in **Fig. 3a**; Stenzel, 1963; Carriker et al., 1979;

396   Sørensen et al., 2012). Close similarities with modern oysters allow to infer that shell growth in *R.*

397   *diluvianum* occurred in a similar way to modern oyster species like *Ostrea edulis*, *Crassostrea virginica* and

398   *C. gigas*. On this basis we could estimate the total shell height at specific times in ontogeny from

399   microstructural growth markers (dashed lines in **Fig. 3a**; following Zimmt et al., 2018), linking growth to

400   changes in shell chemistry.

401   **4.3 Trace element results**

402   The similarity in growth between *R. diluvianum* and modern oyster species is used to assess whether trace

403   element variability in *R. diluvianum* can be interpreted in terms of environmental changes in a similar way

404   as in modern oyster shells (e.g. Surge and Lohmann, 2008; Ullmann et al., 2013; Mouchi et al., 2013;

405   Dellinger et al., 2018). The combination of µXRF and LA-ICP-MS analyses on *R. diluvianum* shells resulted

406   in records of changes in Mg/Ca, Sr/Ca (µXRF), Mg/Li and Sr/Li (LA-ICP-MS) as well as individual

407   concentrations of trace elements such as Mg, Mn, Fe and Sr (**Figure 5**). All chemical analyses were carried

408   out on the dense foliated calcite exposed in cross sections close to the inner edge of the shell valve (**Fig.**

409   **3a**). High-resolution color scans and detailed recording of sampling positions allowed these records to be

410   plotted on a common axis (see **S6**, **S10**). In **Fig. 5**, results of chemical analyses of *R. diluvianum* specimens

411   (including diagenetically altered parts) are compared with data from three other mollusk taxa (the belemnite

412   *Belemnellocamax mammillatus*, the oyster *Acutostrea incurva* and the radiolithid rudist *Biradiolites*

413   *suecicus*) from Ivö Klack (Sørensen et al., 2015), as well as data from extant oysters (Rucker and Valentine,

414   1961; Surge et al., 2001; Ullmann et al., 2013). Multi-proxy analysis revealed periodic variations in stable

415   isotope and trace element ratios (see **Fig. 6**). The amplitudes of these variations plotted in **Fig. 5** show that

416   Mg and Sr concentrations measured in all three fossil bivalve taxa are similar, while concentrations in the

417   belemnite rostra are much higher. Finally, plots in **Fig. 5b** and **Fig. 5d** demonstrate that diagenetic alteration

418   (evident from elevated Mn concentrations) reduces the Sr concentration in carbonate of all four taxa. Stable

419   oxygen isotope ratios of the shells are affected to a lesser degree (see below). The majority of

420   measurements in all four taxa show very little signs of diagenetic alteration, with most measurements

421   characterized by low (< 100 µg/g) Mn concentrations (**Fig. 5**).

422
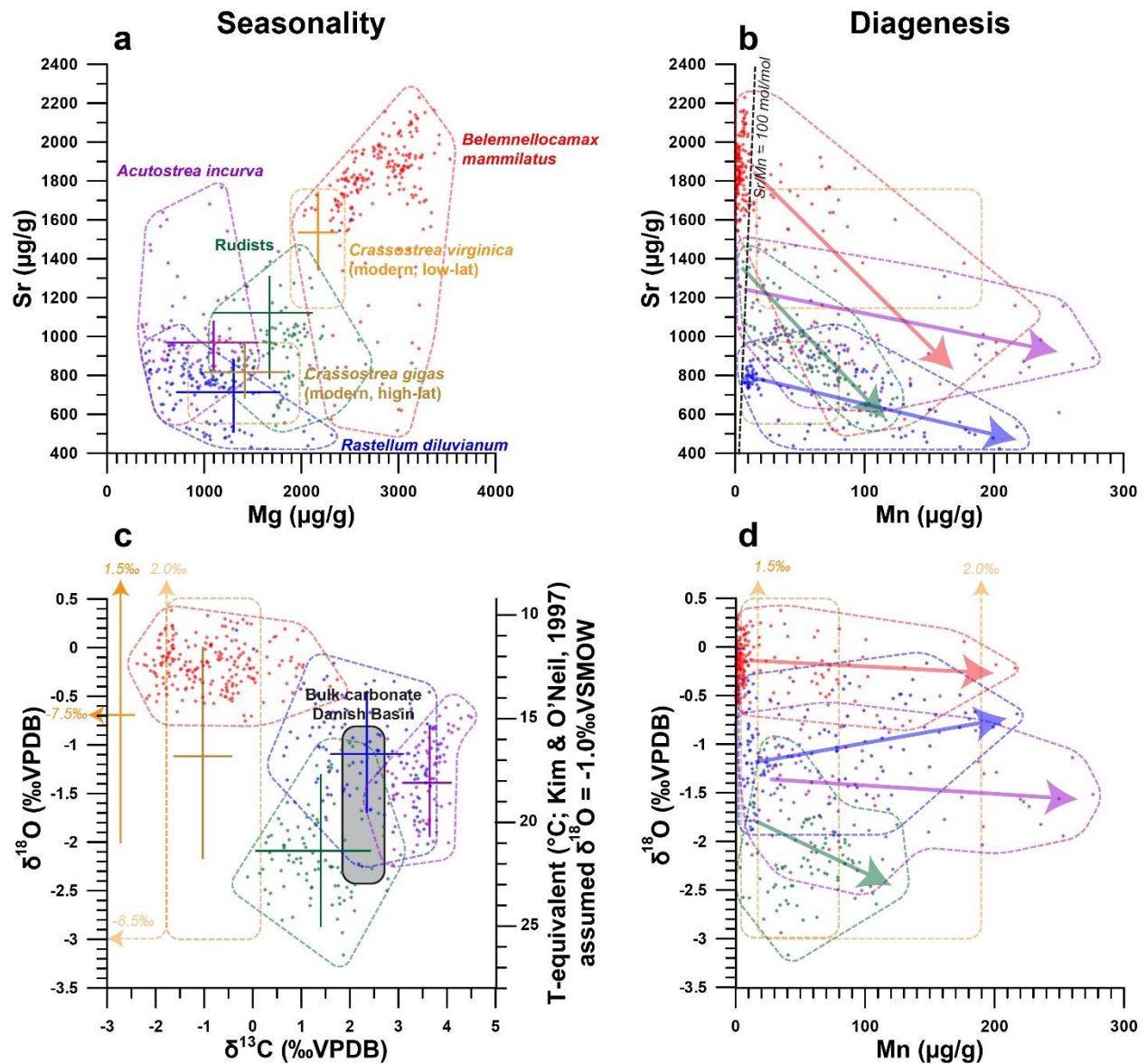
Figure 5: Cross plots summarizing the results of trace element and stable isotope analyses of the oysters *R. diluvianum* (blue), *A. incurva* (purple), the rudist *Biradiolites suecicus* (green) and the belemnite *B. mammilatus* (red, after Sørensen et al., 2015) from the Kristianstad basin. Results from modern *C. gigas* (brown; Ullmann et al., 2013) and *C. virginica* (yellow; Rucker and Valentine, 1961; Surge et al., 2001) oysters are plotted for comparison. Points indicate individual data points, drawn polygons illustrate the range of the data and crosses indicate the extent of seasonality (if present). (**a**) Strontium concentrations plotted against magnesium concentrations. (**b**) Strontium concentrations plotted against manganese concentrations. Arrows indicate the interpreted direction of diagenetic alteration and the black dashed line shows the Sr/Mn diagenesis threshold proposed for belemnite rostra by Sørensen et al. (2015; 100 mol/mol). (**c**) $\delta^{18}O$ plotted against $\delta^{13}C$. Grey area indicates the range of stable isotope ratios measured in Campanian chalk deposits from the nearby Danish Basin by Thibault et al. (2016) (**d**) $\delta^{18}O$ plotted against manganese concentrations, with arrows indicating proposed direction of diagenetic alteration.

A δ^{18}O$_c$ (‰VPDB)

B δ^{13}C$_c$ (‰VPDB)
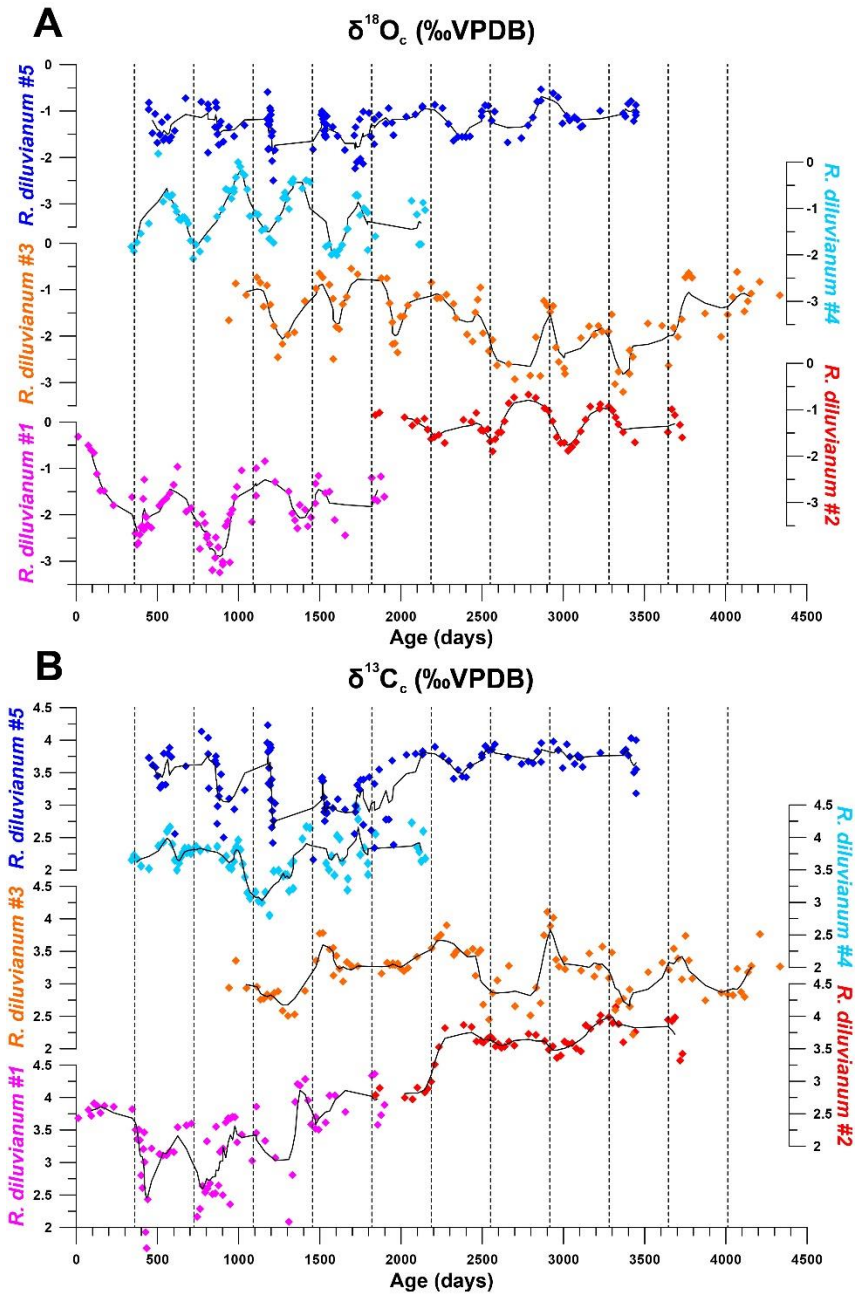
Figure 6: Overview of stable oxygen (**A**) and carbon (**B**) profiles from all five shells in which stable isotope profiles were measured plotted against ontogenetic ages. Black lines indicate 5-point running averages through the time series. Vertical dashed lines separate years of growth. All vertical axes of δ^{18}O and δ^{13}C have the same scale. Colors coding is the same as in **Figure 7**.

4.4 Stable isotope records

An overview of stable isotope results of *R. diluvianum* (IRMS, only for shells 1-5, see **Fig. 2**) compared with the different taxa in Kristianstad Basin and modern oyster data is given in **Figure 5**. Stable isotope ratios of the rudist and oyster shells overlap, while belemnite rostra of the species *B. mammillatus* are characterized by much lower $\delta^{13}C$ and higher $\delta^{18}O$ values. This suggests that $\delta^{13}C$ in belemnite rostra from this species are affected by vital effects while heavier $\delta^{18}O$ values of the belemnites suggest that belemnites lived most of their life away from the coastal environment (in deeper waters), as previously suggested by Sørensen et al. (2015). In contrast, stable isotope ratios recorded in the bivalve shells overlap and match the isotope ratios measured in Campanian chalk deposited in the neighboring Danish Basin (Thibault et al., 2016). Records of $\delta^{13}C$ and $\delta^{18}O$ in the growth direction through *R. diluvianum* shells exhibit periodic variations (**Figure 6**). These variations are much more regular in $\delta^{18}O$ records, which show extreme values below -3‰ and up to 0‰ VPDB (**Fig. 6a**). Some shells, such as *R. diluvianum* 3 (**Fig. 7**), exhibit longer term trends on which these periodic variations are superimposed. These trends suggest the presence of multi-annual cyclicity with a period in the order of 10-20 years, but the length of *R. diluvianum* records (max. 10 years) is smaller than the estimated period of these changes and is therefore insufficient to statistically validate the presence of this cyclicity.

The extreme values in $\delta^{18}O$ records translate to tentative temperatures in the range of extremes of 12°C to 26°C when assuming a constant $\delta^{18}O_{sw}$ value of -1.0‰ (e.g. Thibault et al., 2016) and applying the temperature relationship of Kim and O'Neil (1997). However, the assumption of constant $\delta^{18}O_{sw}$ may add bias to the temperature reconstructions, as seawater composition may not have been constant or reflect the marine value year-round in the nearshore Ivö Klack setting. Carbon isotope ratios ($\delta^{13}C$) do not always follow the same trends as $\delta^{18}O$ records (**Fig. 6b**). In many parts of *R. diluvianum* shells, there is a clear covariation between the two isotope ratios, suggesting $\delta^{13}C$ is affected by seasonal changes. However, in other parts this correlation is less clear, suggesting that other (non-seasonal) factors play a role in determining the $\delta^{13}C$ of shell material.

4.5 Age models

466   Modelling the growth of *R. diluvianum* bivalves from seasonal variations in $\delta^{18}O$ profiles yielded age models,

467   growth rate estimates and reconstructions of water temperature variations during the lifetime of the bivalves.

468   Due to the clear seasonal patterns in $\delta^{18}O$ records (**Fig. 6a**, **Fig. 7**), modelled $\delta^{18}O$ profiles closely

469   approximated the measured $\delta^{18}O$ profiles (total R^2 = 0.86, N = 412, see **S5** and **S9**), lending high confidence

470   to shell age models (see example in **Fig. 7**). Modelling allowed all proxies measured in the shells of *R.*

471   *diluvianum* to be plotted against shell age, clearly revealing the influence of seasonal variations in

472   environmental parameters on shell chemistry (**S10**). The age models reveal clear, statistically significant (p

473   < 0.05) ontogenetic trends in Mg/Li, Sr/Li and $\delta^{13}C$ in nearly all specimens of *R. diluvianum* (see **Table 1**).

474   In 3 out of 5 shells, $\delta^{13}C$ increases with age (see **Fig. 6b** and **Table 1**) with ontogenetically older specimens

475   (e.g. *R. diluvianum* #2) yielding overall higher $\delta^{13}C$ values (**Fig. 6b**). The distribution of slopes of ontogenetic

476   trends in Li/Ca cannot be distinguished from random variation. Therefore, no widely-shared ontogenetic

477   trends were found for Li-proxies in *R. diluvianum* shells.

478

	Li/Ca			$\delta^{13}C$		
	slope (mol/(mol*yr))	R2	p-value	slope (‰/yr)	R2	p-value
R. diluvianum 1	-1.29E-06	0.053	4.32E-08	0.346	0.426	8.86E-07
R. diluvianum 2	3.74E-07	0.101	2.68E-05	0.169	0.440	8.19E-08
R. diluvianum 3	3.86E-07	0.004	5.32E-03	-0.004	0.001	8.09E-01
R. diluvianum 4	-1.07E-06	0.025	8.78E-04	0.023	0.009	3.99E-01
R. diluvianum 5	-1.94E-06	0.030	6.30E-14	0.136	0.492	5.53E-11
R. diluvianum 6	-2.32E-06	0.117	8.75E-15			
R. diluvianum 7	-7.49E-07	0.029	4.77E-02			
R. diluvianum 8	-1.19E-07	0.003	2.90E-01			
R. diluvianum 9	-4.63E-07	0.010	5.65E-02			
R. diluvianum 10	1.59E-06	0.015	1.61E-02			
R. diluvianum 11	-1.87E-06	0.199	4.25E-12			
R. diluvianum 12	-4.55E-07	0.003	4.19E-01			

$p(\chi^2)$	0.976	$p(\chi^2)$	1.000
$p(\chi^2)$ weighed by R2	0.976	$p(\chi^2)$ weighed by R2	1.000
$p(\chi^2)$ weighed by p-value	0.961	$p(\chi^2)$ weighed by p-value	0.998

479

480 **Table 1:** *Overview of the slopes of ontogenetic trends in Li/Ca and $\delta^{13}C$ records. P-values on the bottom of the table show that the*

481 *distribution of Li/Ca slopes is statistically indistinguishable from random.*
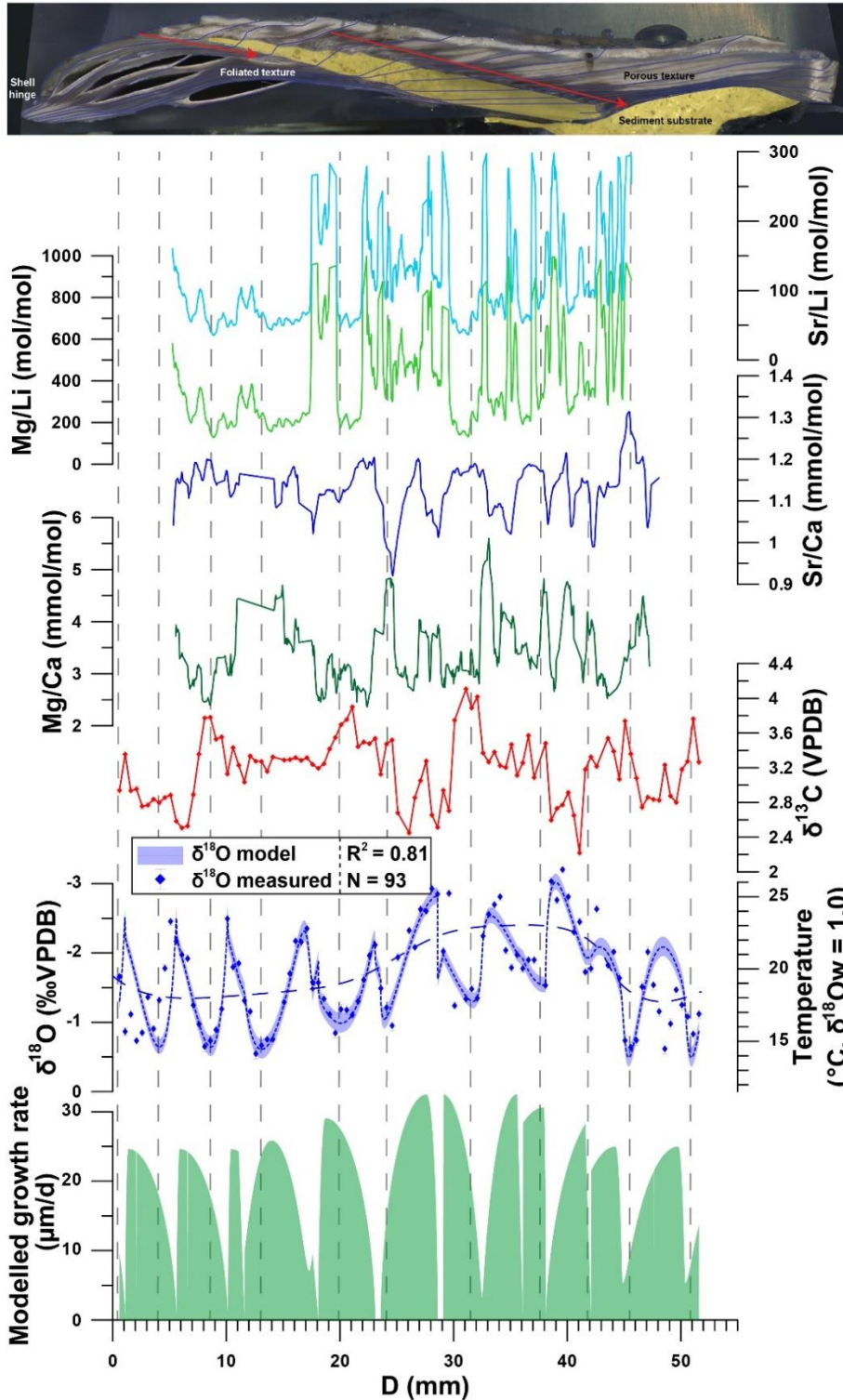
482

Figure 7: Example of multi-proxy records measured in *R. diluvianum* specimen 3 plotted against distance in growth direction (see image on top and **Fig. 3** for reference). From top to bottom, records of Sr/Li (light blue), Mg/Li (light green), Sr/Ca (dark blue), Mg/Ca (dark green), δ^{13}C (red), δ^{18}O (blue dots with error bars) and modelled growth rate (light green fill) are plotted. The shaded blue curve plotted underneath the δ^{18}O record illustrates the result of growth and δ^{18}O modelling and its propagated error (vertical thickness of curve, 2SD). The dashed blue curve plotted on top of the δ^{18}O record shows the observed multi-annual trend in the data. Vertical dashed lines separate growth years. Multi-proxy plots for all specimens are given in **S10**.

483

5. Discussion

5.1 Preservation

The relative lack of burial and tectonic activity in the Kristianstad Basin has provided ideal circumstances for the nearly immaculate preservation of *R. diluvianum* shells in the Ivö Klack locality (Kominz et al., 2008; Surlyk and Sørensen, 2010). The excellent state of these shells is evident by the preservation of original (porous and foliated) microstructures that closely resemble those reported for several species of modern ostreid shells (Carriker et al., 1979; Surge et al., 2001; Ullmann et al., 2010; 2013; Zimmt et al., 2018; **Fig. 2-3**). High magnification SEM images demonstrate the excellent preservation of foliated and vesicular calcite structures in *R. diluvianum* shells (**Fig. 3b-d**). The preservation state of *R. diluvianum* shells meets the SEM-based preservation criteria for robust stable isotope analysis set by Cochran et al. (2010). MicroXRF mapping reveals that the foliated calcite in the shells is characterized by high Sr concentrations and low concentrations of Mn, Fe and Si, elements which are generally associated with diagenetic alteration (e.g. Brand and Veizer, 1980; Al-Aasm and Veizer, 1986a; Immenhauser et al., 2005; **Fig. 3b-h**). Trends in bulk Mn and Sr concentrations observed in all fossil species from Ivö Klack (**Fig. 5b;** including less well-preserved parts) likely point towards a diagenetic process affecting a less well-preserved subset of the data. The lack of covariation between Mn concentration and $\delta^{18}O$ shows that there is little evidence for meteoric diagenesis in these shells (**Fig. 5d**; Ullmann and Korte, 2015). Instead, these patterns are best explained by early marine cementation of porous carbonate structures from sea water with similar temperature and $\delta^{18}O$ as the living environment (see also Sørensen et al., 2015).

Typically, a Mn concentration threshold of 100 µg/g is applied below which Cretaceous low-magnesium carbonates are assumed suitable for chemical analysis (Steuber et al., 2005; Huck et al., 2011). Strontium concentrations above 1000 µg/g have also been used as markers for good preservation, since diagenetic processes can cause strontium to leach out of carbonates (e.g. Brand and Veizer, 1980; Huck et al., 2011; Ullmann and Korte, 2015). Previous studies of belemnites in Kristianstad Basin proposed a molar Sr/Mn threshold of 100 for belemnite rostra (Sørensen et al., 2015). However, the height of thresholds used for diagenetic screening differs widely in the literature due to variation between species, fossil matrices and burial histories (e.g. Veizer, 1983; Steuber et al., 1999; Ullmann and Korte, 2015; de Winter and Claeys,

511   2016). Applying these thresholds risks introducing biases to chemical datasets from fossil shells and may

512   not be an ideal method for diagenetic screening. Furthermore, large variation in the *in vivo* incorporation of

513   Mn and Sr in mollusk shell carbonate and a strong dependence on the diagenetic setting can make the

514   interpretation of shell preservation from trace element ratios alone highly ambiguous (Ullmann and Korte,

515   2015). The complex patterns in multi-proxy datasets in this study (**Fig. 5**) merit great care in applying simple,

516   general thresholds for grouping different processes of carbonate diagenesis. Therefore, in this study, a

517   multi-proxy approach is applied for diagenetic screening in which data is excluded based on a combination

518   of Si, Ca, Mn, Fe and Sr concentrations, $\delta^{18}O$ values as well as SEM and visual observations of the shell

519   structure at the location of measurement.

520   **5.2 Dating the Ivö Klack locality**

521   While previous attempts at dating Campanian strata mainly focused on relative dating using magneto- and

522   biostratigraphy (Montgomery et al., 1998; Jarvis et al., 2002; Voigt et al., 2010), integration of

523   cyclostratigraphic approaches has recently allowed to constrain the age of the Campanian deposits more

524   precisely (Voigt and Schönfield, 2010; Thibault et al., 2012; Wendler, 2013; Thibault et al. 2016).

525   Unfortunately, these rarely cover the time interval in which the Ivö Klack sediments were deposited (e.g.

526   Wendler, 2013; Perdiou et al., 2016). Strontium isotope dating places the Ivö Klack deposits at 78.14 ± 0.26

527   Ma (**Fig. 4**), slightly above the early/late Campanian boundary, while the *B. mammilatus* biozone is defined

528   as late early Campanian (Wendler, 2013). Influx of radiogenic strontium-rich weathering products from the

529   nearby Transscandinavian Igneous Belt may bias age estimates from strontium isotope ratios (Högdahl et

530   al., 2004). However, studies of modern strontium isotope ratio variability (Palmer and Edmond, 1989) and

531   the potential bias of strontium isotope ratios in shallow-water carbonates (Kuznetsov et al., 2012; El

532   Meknassi et al., 2018) show that the effect of such inputs on strontium isotope dating results is generally

533   negligible, except in semi-confined shallow-marine basins characterized by considerable freshwater input

534   and low salinities (<7 psu). No evidence exists for such exceptional conditions at Ivö Klack (see **2.1**). We

535   therefore conclude that our strontium isotope age estimate, together with biostratigraphic constraints,

536   places the Ivö Klack locality in the earliest late Campanian. The refined dating of the Ivö Klack deposits and

537   fossils allows the results of sclerochronological investigations presented in this work to be placed in the

538   context of longer-term climate reconstructions with improved precision.

5.3 Trace element variability

Extracted ranges in seasonal scale periodic variability in Mg/Ca, Sr/Ca, Mg/Li and Sr/Li in all 12 *R. diluvianum* shells (**Fig. 8**) show that it is not straightforward to interpret these records in terms of temperature changes. Some of this difficulty arises from the large inter-shell variability in trace element ranges, mostly expressed in strong positive correlations between Sr/Li and Mg/Ca (R^2 = 0.76) and between Sr/Li and Mg/Li (R^2 = 0.93). The benthic foraminifera proxy transfer function for Mg/Li (Bryan and Marchitto, 2008) does not work for *R. diluvianum* (temperatures >50°C), presumably due to typically lower Mg concentrations in foraminifera compared to bivalves (Yoshimura et al., 2011). Bivalve-specific temperature relationships of Mg/Ca (Surge and Lohmann, 2008; based on *Crassostrea virginica*), Sr/Li (Füllenbach et al., 2015; based on *Cerastoderma edule*) and Mg/Li (Dellinger et al., 2018; based on *Mytilus edulis*) yield temperatures in the same range as those reconstructed from stable oxygen isotope measurements (10-20°C). However, Sr/Li-based temperature trends are opposite to those based on Mg-proxies, suggesting that they cannot both be applicable to *R. diluvianum*. Poorly constrained changes in seawater chemistry (Mg/Ca and Sr/Ca ratios of ocean water) also hinder these trace element-based reconstructions (Lear et al., 2003; Coggron et al., 2010; Rausch et al., 2013). The strong Mg/Li-Sr/Li correlation indicates that both proxies are likely strongly affected by the specimen-specific ontogenetic trends in Li/Ca described in **Table 1**. This, together with the large inter-specimen variability shows that both Li-proxies cannot be used as temperature proxies in *R. diluvianum*. An annual stack of all proxies shows that the positive correlation between Mg/Ca and $\delta^{18}O$ (**Fig. 9**) is opposite to the temperature-relationships found in modern oyster species (Surge and Lohmann, 2008; Mouchi et al., 2013; Ullmann et al., 2013). This together with the reduced seasonal variability (1.2 mmol/mol versus 4-10 mmol/mol in modern oysters; Surge and Lohmann, 2008; Mouchi et al., 2013) and the large (>3 mmol/mol; **Fig. 8**) inter-specimen variability both in mean value and seasonal Mg/Ca range rules out Mg/Ca as a reliable temperature proxy in *R. diluvianum*. This result demonstrates that earlier successful attempts to establish calibration curves for Li- and Mg-based temperature proxies (e.g. Füllenbach et al., 2015; Dellinger et al., 2018) are probably strictly limited to these bivalve species or close relatives. The same conclusion was also drawn by Dellinger et al. (2018) based on Li/Mg and Li isotope ratio measurements in biogenic carbonates. The lack of Mg/Li or Sr/Li calibrations in modern oyster shells limits the interpretation of our results for these element ratios. Establishing such

567 calibrations using modern oysters in cultured experiments may allow these proxies to be used for

568 reconstructions from fossil oyster shells in the future.

569 While not a promising candidate for reconstructing temperature (Gillikin et al., 2005; Schöne et al., 2013;

570 Ullmann et al., 2013), seasonal Sr/Ca fluctuations and relationships between Sr/Ca and $\delta^{18}O$ are consistent

571 between individuals (**Fig. 8-9**; see also **S6**). This allows Sr/Ca ratios to be used together with microstructural

572 observations of growth increments as a basis for seasonal-scale age models in shells for which no $\delta^{18}O$

573 measurements were done. Both mean Sr/Ca values and seasonal variability in *R. diluvianum* are consistent

574 with those observed in the same microstructure in modern *Crassostrea gigas* growing in a similar

575 environment (0.8-1.0 mmol/mol; Ullmann et al., 2013), suggesting a consistent incorporation of Sr by

576 different oyster taxa over time. It must be noted that one should be cautious when directly comparing trace

577 element concentrations in biogenic calcite between different time periods, as the seawater composition of

578 Late Cretaceous oceans (e.g. concentrations of Mg, Ca, Sr and especially Li) may have been different from

579 that of the present-day ocean (Stanley and Hardie, 1998; Coggon et al., 2010; Rausch et al., 2013). Local

580 enrichments in seawater Sr concentrations at Ivö Klack driving increased Sr content in *R. diluvianum* are

581 unlikely, since Sr/Ca ratios exhibit only small (2-3%) lateral variability in the world's oceans (De Villiers,

582 1999). Because Sr/Ca ratios in Late Cretaceous oceans were half those of the modern ocean, one would

583 expect that Sr concentrations in Late Cretaceous biogenic carbonate would be half those in carbonates

584 formed in the modern ocean, if the partition coefficient between seawater concentrations and shell

585 concentrations has remained constant (Stanley and Hardie, 1998; de Winter et al., 2017a). The fact that

586 this reduction in Sr concentrations relative to the modern ocean is not observed in *R. diluvianum* may mean

587 that there is a physiologically fixed concentration of Sr in an oyster's shell that is independent of ambient

588 Sr concentrations.

589
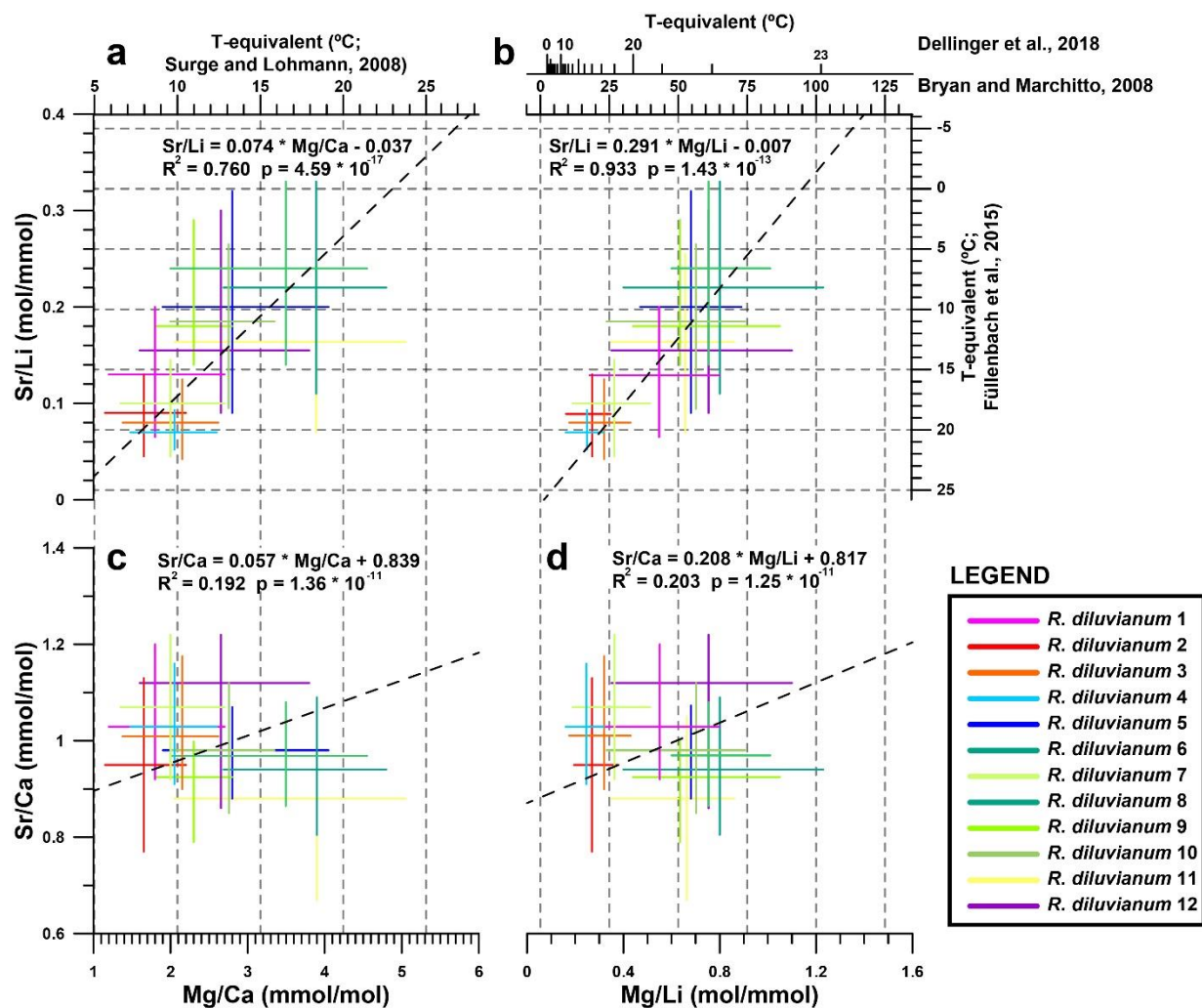
Figure 8: Cross plots showing the extent of interpreted seasonality observed in records of four trace element proxies in all 12 *R. diluvianum* specimens. Colors of lines of individual shells correspond to colors indicated in **Fig. 2**. Temperature conversions from previously published regressions of the proxies with temperature are shown on opposite axes with grey dashed lines corresponding to major tick marks on the temperature scale (**a**) Sr/Li plotted against Mg/Ca showing a strong significant intra-shell correlation. (**b**) Sr/Li plotted against Mg/Li showing a strong significant intra-shell correlation due to dominant variations in Li concentration. Note that two different Mg/Li temperature calibrations were explored. (**c**) Sr/Ca plotted against Mg/Ca showing weak but significant intra-shell correlation. (**d**) Sr/Ca plotted against Mg/Li showing a weakly significant intra-shell correlation. Data for this plot is found in **S13**.
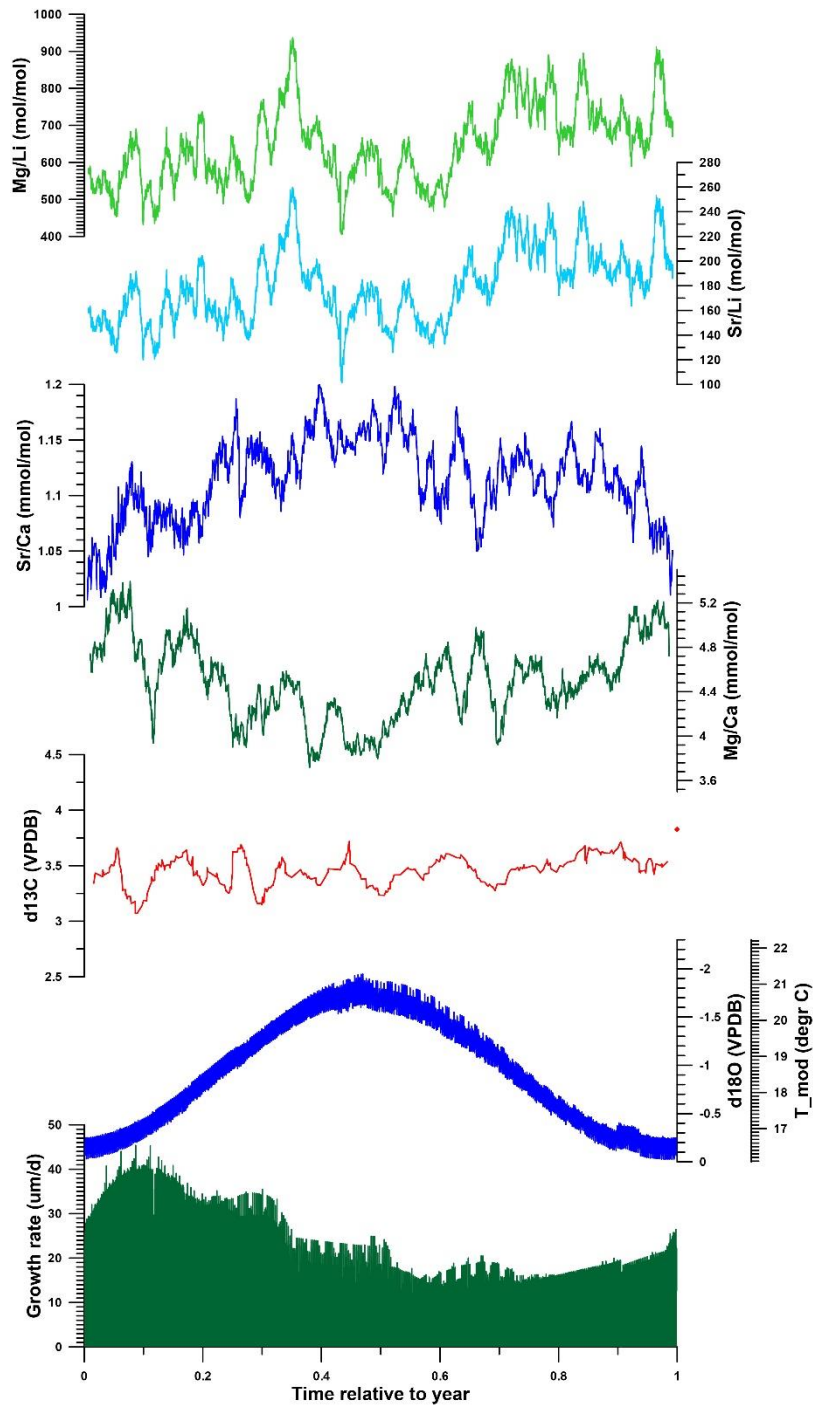
600

Figure 9: Composite of multi-proxy records from all *R. diluvianum* shells stacked and plotted on a common time axis of 1 year to illustrate the general phase relationships between various proxies in the shells. Records were colored as in **Fig. 7**. Annual stacks plotted in this figure were produced by applying age models on all multi-proxy records, plotting all results against their position relative to the annual cycle and applying 20 point moving averages.

601

5.4 Temperature seasonality

602

603 An annual stack of all *R. diluvianum* proxy records shows a $\delta^{18}O_c$-based temperature variability in Ivö Klack

604 of 16-21°C when assuming a constant $\delta^{18}O_{sw}$ of -1‰VSMOW (**Fig. 6**). However, comparison with $\delta^{18}O$-

605 seasonality in individual specimens shows that the annual stack severely dampens seasonality due to small

606 phase shifts in maximum and minimum temperatures, small uncertainties in the age models between years

607 and specimens, and inter-annual differences and longer-term trends in temperature (see **Fig. 6**). A more

608 accurate estimate of the seasonal extent is obtained by calculating the seasonal range from the coolest

609 winter temperatures (12.6°C in *R. diluvianum* 4; **Fig. 6**; **S10**) with the warmest recorded summer

610 temperature (26°C in *R. diluvianum* 1; **Fig. 6**; **S10** which yields an extreme maximum seasonal sea surface

611 temperature (SST) range of ±13.4°C.

612 A complication of these reconstructions is the assumption of constant $\delta^{18}O_{sw}$ of -1‰VSMOW, which is

613 unlikely to be completely accurate in the nearshore Ivö Klack locality. Comparison with data from

614 *Crassostrea gigas* growing in a similar nearshore environment (Ullmann et al., 2010; German North Sea

615 coast, 54°N) show that such an environment away from large river mouths can typically experience

616 seasonal salinity fluctuations of ~4 psu resulting in a dampening of the seasonal $\delta^{18}O_c$ cycle by

617 ~0.5‰VPDB. Such a salinity-effect would reduce our reconstructed 13-26°C seasonal temperature range

618 by ~2°C to 14-25°C.

619 In addition, mean annual $\delta^{18}O_{sw}$ values can be considerably lower than the global average seawater

620 composition (e.g. -1‰ to -1.5‰VSMOW compared to global ocean mean of 0‰VSMOW in Ullmann et al.,

621 2010). Considering such a deviation would reduce reconstructed temperatures by 4-6°C to 10-21°C, much

622 colder than open marine reconstructions of the Boreal Chalk Sea by Thibault et al. (2016). This result would

623 be in strong disagreement with a recent study by Tagliavento et al. (2019) in which clumped isotope

624 analyses (which do not rely on the assumption of constant $\delta^{18}O_{sw}$) were used to correct the $\delta^{18}O_c$-based

625 reconstructions of the Boreal Chalk, and yielded *higher* temperatures (~26°C MAT for open marine SST)

626 and a correction of $\delta^{18}O_{sw}$ towards 1-1.5‰ heavier values (resulting in a Campanian $\delta^{18}O_{sw}$ of -

627 0.5-0‰VSMOW). Another caveat is that salinity effects on local $\delta^{18}O_{sw}$ strongly depend on the local $\delta^{18}O_{sw}$

628 of the local freshwater source (riverine or precipitation), which in the present-day higher mid-latitudes is

629 around -7‰VSMOW to -8‰VSMOW (e.g. Ullmann et al., 2010), but this is impossible to constrain at Ivö

630 Klack during the Campanian within the scope of this study.

631 If local $\delta^{18}O_{sw}$ values at Ivö Klack were indeed 1-1.5‰ reduced with respect to those in the fully marine

632 Boreal Chalk Sea, and marine $\delta^{18}O_{sw}$ was around 0-0.5‰VSMOW rather than the assumed -1‰VSMOW,

633 the effects of these two biases cancel each other out, and the best estimation of the extreme seasonal SST

634 range at Ivö Klack based on this study's data would be 14-25°C with a MAT of 19°C. This MAT is

635 comparable to the MAT of the late early Campanian Boreal Chalk Sea waters of 17-19°C calculated from

636 coccolith-$\delta^{18}O_c$ (Lowenstam and Epstein, 1954; Jenkyns et al., 2004; Friedrich et al., 2005; Thibault et al.,

637 2016), and slightly warmer than mean annual air temperatures from this paleolatitude based on phosphate-

638 $\delta^{18}O$ reconstructions (±15°C; Amiot et al., 2004). However, Ivö Klack SST's are ~6°C colder than the

639 clumped isotope-based reconstructions from marine chalk samples (Tagliavento et al., 2019). The latter

640 could indicate that coastal SST's and air temperatures were much colder than marine temperatures in the

641 Campanian higher latitudes, but such temperature differences are highly unusual compared to modern

642 climates. Alternatively, this difference could highlight a severe temperature bias in (both phosphate and

643 carbonate) $\delta^{18}O$-based reconstructions, which should be further investigated using independent marine

644 temperature proxies such as the clumped isotope paleothermometer (e.g. de Winter et al., 2018;

645 Tagliavento et al., 2019).

646 Modelled growth rates in *R. diluvianum* peak near the end of the low temperature season and average

647 growth rates are lowest shortly after the temperature maximum (**Fig. 9**). This phase shift between

648 temperature and growth rate could indicate that growth in *R. diluvianum* in this setting was not limited by

649 low temperatures, as observed in modern mid- to high-latitude oysters (Lartaud et al., 2010). High

650 temperature extremes (>25°C) may have slowed or stopped growth, as recorded in modern low latitude

651 settings (Surge et al., 2001). Heat shock has been shown to limit the growth of modern oysters (*Crassostrea*

652 *gigas*; Li et al., 2007), although the relatively moderate SST seasonality suggests that very high (>25°C)

653 temperatures were not common at the Ivö Klack locality (**Fig. 6**). In this respect it is important to recognise

654 that the use of $\delta^{18}O$ records from multiple specimens reduces the effects of growth cessations of individuals

655 on seasonal SST reconstructions and allows the full seasonal range in SST to be resolved.

656   The reconstructed MAT for Ivö Klack is 7-8 degrees warmer than the present-day seasonal SST range in

657   the North and Baltic seas at similar latitude (e.g. 2-18°C monthly seasonality range in Baltic Sea Karlskrona,

658   Sweden, 56°N and 4-18°C monthly seasonality range in North Sea Esbjerg, Denmark, 55°N; IRI/LDEO

659   Climate Data Library, 2020). Seasonal SST range at Ivö Klack (11°C) is significantly lower than the 14-

660   16°C maximum seasonal range in temperature that occurs in the present-day Baltic and North seas

661   (IRI/LDEO Climate Data Library, 2020). Data on temperature seasonality in the Late Cretaceous are scarce,

662   especially in high-latitude settings. However, comparison with data on Cretaceous temperature seasonality

663   between 15°N and 35°N paleolatitude (Steuber et al., 2005) shows that while MAT at 50°N was significantly

664   lower than at lower latitudes (19°C and 25-30°C, respectively), the seasonal temperature range during

665   cooler periods in the Late Cretaceous was remarkably similar between latitudes (10-15°C in subtropical

666   latitudes vs. ±14°C in this study). This observation contrasts with the present-day situation in Northern

667   Africa and Europe, in which seasonal temperature ranges are generally much higher in mid- to high-

668   latitudes (30-50°N) than in lower latitudes (10-30°N; Prandle and Lane, 1995; Rayner, 2003; Locarnini et

669   al., 2013; NOAA, 2020). Our SST reconstructions also show that Late Cretaceous latitudinal temperature

670   gradients and mid- to high-latitude seasonality were larger than previously assumed based on climate

671   model results (Barrera and Johnson, 1999; Hay and Floegel, 2012; Upchurch et al., 2015).
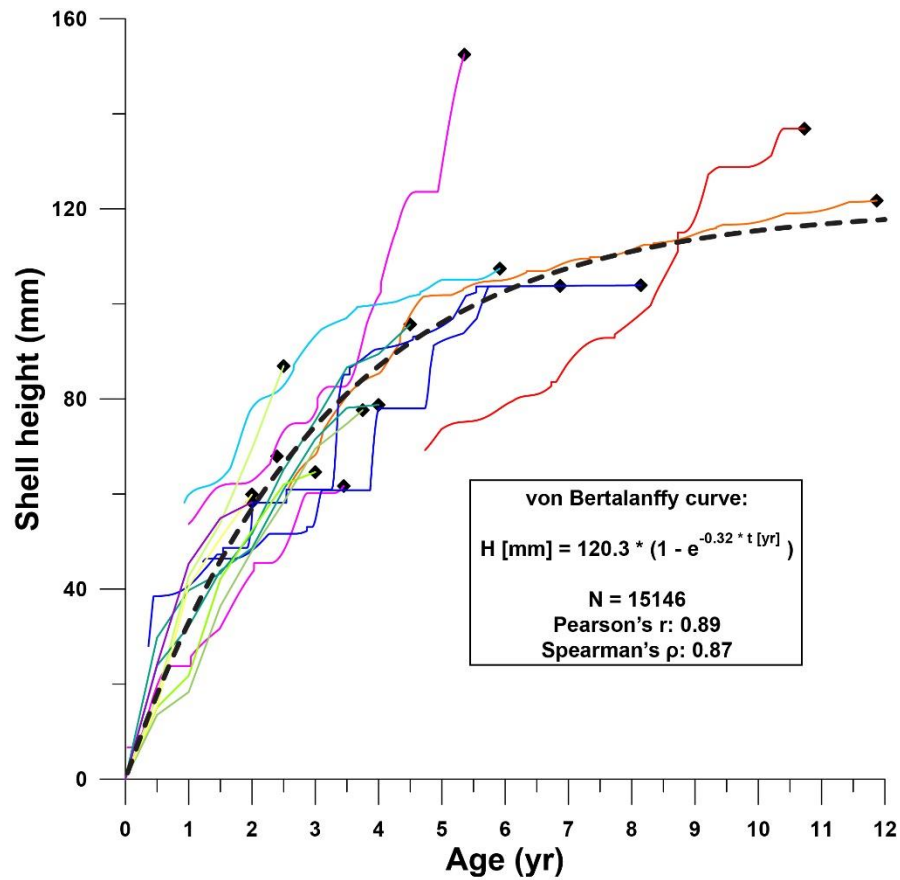
672   **5.5 Shell growth and ontogeny**

673   5.5.1. Growth curves

674   Growth curves of individual *R. diluvianum* specimens clearly converge to a general growth development

675   curve for the species (**Fig. 10**). Considering that these growth curves are based on δ^{18}O and Sr/Ca transects

676   in different stages of life in different specimens (large age variation; see **Fig. 8**), individual growth curves

677   are remarkably similar. The growth of *R. diluvianum* takes the typical shape of the asymptotic Von

678   Bertalanffy curve, in which shell height (H_t) development with age (*t*) is related to a theoretical adult size

679   H_{max} and a constant *k* in the equation: $H_t[mm] = H_{max} * (1 - e^{k*(t[yr]-t_0)})$, with t_0 representing the time at

680   which the growth period started (always zero in this case; von Bertalanffy, 1957). When this formula is

681   regressed over all modelled growth data of all shells (1 data point per day, 15146 points in total), the fit with

682   an H_{max} of ±120.3 mm and a K value of ±0.32 is very good (R^2 = 0.79; see **Fig. 10**).

683   The consistency in growth curves between individuals of *R. diluvianum* is surprising as modern oyster

684   species are known to exhibit large variations in growth rates and shell shapes as a function of their colonial

685   lifestyle, which often limits the growth of their shells in several directions (Galtsoff, 1964; Palmer and

686   Carriker, 1979). The strong resemblance of growth between individuals and the close fit of the idealized

687   von Bertalanffy growth model suggests that growth of *R. diluvianum* at Ivö Klack was relatively unrestricted

688   in space. This hypothesis is consistent with the apparent mode of life of *R. diluvianum* in Ivö Klack,

689   cemented next to each other in loose groups, subject to strong wave action and turbulence, such that

690   individuals received the same (high) supply of food (Surlyk and Christensen, 1974; Sørensen et al., 2012).

691   The shape of the growth curve of *R. diluvianum* resembles that of modern Chesapeake Bay oysters

692   (*Crassostrea virginica*), which exhibit a slightly larger modelled maximum height (150 mm) and a slightly

693   smaller K-value (0.28). A larger subset of *R. diluvianum* specimens studied by Sørensen et al. (2012)

694   demonstrates that these bivalves could grow up to 160 mm in height. The curvature of the growth curve of

695   *R. diluvianum* (K-value) is also similar to that found for other modern shallow marine bivalve species (e.g.

696   *Macoma balthica*, K = 0.2-0.4; Bachelet, 1980; *Pinna nobilis*, K = 0.33-0.37; Richardson et al., 2004) and

697   significantly higher than in growth curves of deep shelf-dwelling bivalves (e.g. *Placopecten magellanicus*,

698   K = 0.16-0.24; MacDonald and Thompson, 1985; Hart and Chute, 2009) or bivalves from cold habitats (e.g.

699   North Atlantic *Arctica islandica*, K = 0.06; Strahl et al., 2007). This reflects the high growth rates (steeper

700   growth curves, higher K-values) of shallow marine bivalves compared to species living in less favorable

701   (colder or deeper) habitats, with *R. diluvianum* clearly being part of the former group.

702

The figure shows a plot with the following content:

- Y-axis: **Shell height (mm)**, ranging from 0 to 160
- X-axis: **Age (yr)**, ranging from 0 to 12

Text box within the figure:

von Bertalanffy curve:

$H \text{ [mm]} = 120.3 * (1 - e^{-0.32 * t \text{ [yr]}})$

N = 15146
Pearson's r: 0.89
Spearman's ρ: 0.87

703

704 **Figure 10**: Shell height plotted against age for all *R. diluvianum* records (see **Fig. 8** for color legend of lines representing individuals).

705 The similarity between growth curves of different specimens allows a von Bertalanffy curve to be fitted to the data with high confidence.

706 Sinusoidal patterns superimposed on all growth curves are caused by seasonal variability in growth rate (see **Fig. 6-7**). Data found in

707 **S9**.

708

37

5.5.2 Seasonal growth

710 To study variability in minimum growth temperature (**Fig. 11a**), length of the growth season and time of

711 year at which maximum growth occurs (**Fig. 11b**), we isolated individual growth years from all age models

712 of the five shells in which $\delta^{18}O$ curves were measured (**Fig. 11**). The onset and end of each growth year

713 correspond to maxima in $\delta^{18}O$ values (minima in temperatures). The onset of the first growth year in each

714 shell at its precise position relative to the seasonal temperature cycle showed in which season the individual

715 settled and started growing its shell (**Fig. 11b**). All data used to create plots in **Fig. 11** are provided in **S14**.

716 Relationships between these growth parameters are summarized in **Table 2**.
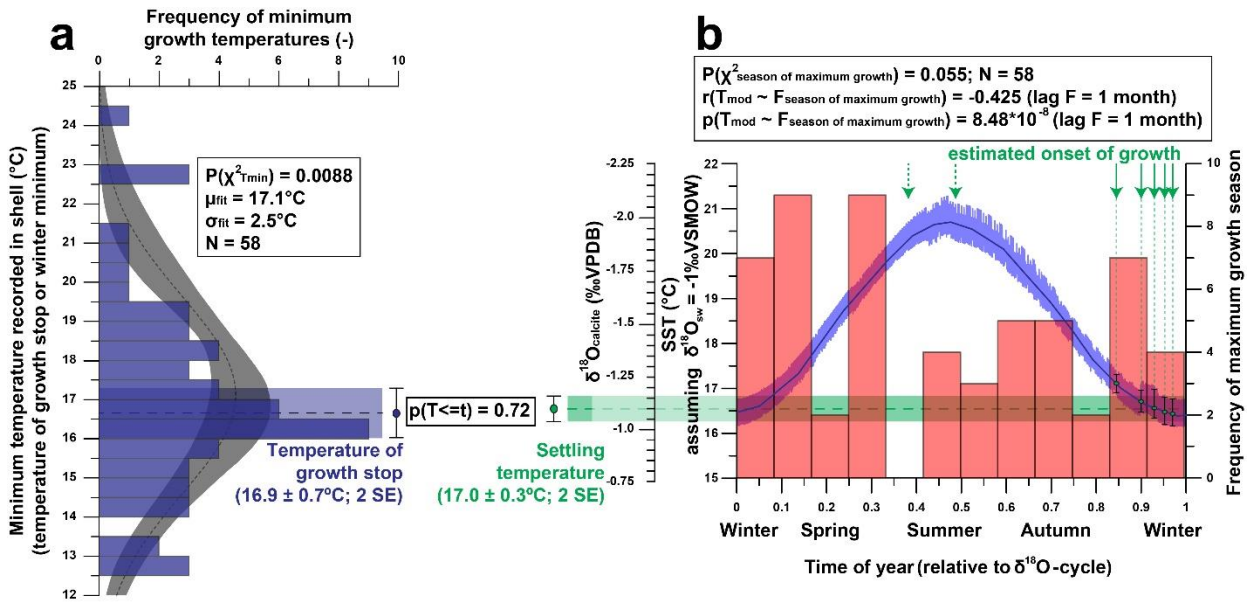
717

718 ***Figure 11:*** Overview of statistical evaluation of growth parameters of *R. diluvianum* derived from age modelling in shells 1-5. (**a**)

719 Histogram of minimum temperatures of growth (equivalent to the time at which growth stops or the minimum yearly temperature) in

720 *R. diluvianum* showing that the temperature at which growth slows coincides with the time of first growth at post-larval settlement (p

721 = 0.717). (**b**) Histogram of the season of maximum growth relative to the $\delta^{18}O$ seasonality cycle shows no significant concentration

722 towards a favorable growing season while moments of first growth (following settlement after the larval stage) are significantly

723 concentrated towards the high-$\delta^{18}O$ season.

N = 58	Total annual growth (µm)		Maximum growth rate (µm/d)		Length of growth season (d)		Minimum growth temperature (°C)		Temperature seasonality (°C)		Average temperature (°C)	
Temperature seasonality (°C)	R^2 0.024		R^2 0.053		R^2 **0.403**							
	p $2.16*10^{-11}$		p $6.73*10^{-10}$		p $2.15*10^{-22}$							
Average temperature (°C)	R^2 0.020		R^2 0.027		R^2 0.008		R^2 **0.565**					
	p $2.29*10^{-11}$		p $6.95*10^{-7}$		p $2.87*10^{-21}$		p $3.44*10^{-7}$					
Age (yr)	R^2 0.000		R^2 0.062		R^2 0.002		R^2 0.002		R^2 0.059		R^2 0.000	
	p $1.11*10^{-9}$		p $9.74*10^{-12}$		p $1.59*10^{-22}$		p $1.05*10^{-30}$		**p 4.59*10⁻¹**		p $1.09*10^{-35}$	

724

Table 2: Overview of statistical evaluation of growth parameters of *R. diluvianum* derived from age modelling in shells 1-5. Coefficients of determination (R^2) and p-values were determined for relationships between temperature seasonality, average temperature, age of the bivalve, length of the season, minimum growth temperatures and annual average and maximum growth rates. Values in green indicate strong correlations while values in red indicate the absence of a correlation. Data reported in **S14**.

The growing season is shorter than 365 days in all but five modelled years, demonstrating that growth stops or slowdowns did occur in *R. diluvianum*. Minimum growth temperatures (temperatures at which growth stopped) are concentrated around 17°C (χ^2 = 0.0088; **Fig. 11a**) and correlate strongly to MAT (R^2=0.57; **Table 2**), suggesting that growth halts in *R. diluvianum* were not forced by an absolute temperature threshold, but rather by timing relative to the seasonality (circadian rhythm). If there had been a fixed temperature threshold (e.g. 6°C or 10°C for *Crassostrea gigas*; Lartaud et al., 2010; Ullmann et al., 2010) the length of the growth season would have positively correlated with annual mean temperature, but this is not the case (R^2<0.1). Other authors have suggested growth in modern *C. gigas* does not actually cease completely but rather slows down significantly, which may also have been the case in *R. diluvianum*. On average, the moment of minimum growth in *R. diluvianum* occurs right after the highest temperatures of the year are reached (early autumn, **Fig. 9**).

The season of first growth (after larval stage) is concentrated in the two last months before the δ^{18}O maximum (first half of winter) when modelled water temperatures are ±17°C (**Fig. 11b**). Note that only three of the five shells allowed sampling of the first month of growth, and extrapolated records for the other two shells are likely unreliable. Comparing **Fig. 11a** and **Fig. 11b** shows that growth halts and settling occur at similar temperatures (16.9 ± 0.7°C and 17.0 ± 0.3°C respectively, p = 0.72), suggesting that these events occur simultaneously or on either side of a seasonal growth halt (if it occurs). The timing of spawning and settling in *R. diluvianum* differs from that in modern oysters, which generally spawn during the spring season, with the young oyster spat settling in the summer (e.g. for *Crassostrea gigas*: Fan et al., 2011). If the larval stage of *R. diluvianum* lasted as long, this would put the spawning season of *R. diluvianum* in

749 summer. In the case of modern oysters, it is known that reproduction requires a relatively warm minimum

750 temperature (ideally around 22°C for *C. gigas*; Cognie et al., 2006), and that a combination of salinity and

751 temperature conditions is important (Fan et al., 2011), while extreme temperatures (>28°C; Surge et al.,

752 2001) can induce shock. Similar temperature conditions occurred at Ivö Klack in summer, possibly

753 explaining the delay of the spawning season of *R. diluvianum*.

754 **Figure 11b** shows that the distribution of months with fastest growth rate is random (p(χ^2) = 0.055, <95%

755 confidence). However, in 27 of the 58 years, the growth peak occurs in the season with decreasing $\delta^{18}O$

756 values ("spring season"). **Table 2** shows that the extent of temperature seasonality (difference between

757 minimum and maximum $\delta^{18}O$ converted to temperature) significantly influences the length of the growing

758 season (R^2 = 0.40). However, total annual growth and maximum growth rates are independent of SST (both

759 seasonal range and MAT) and ontogenetic age of the organism does not predict a significant part of any of

760 the above-mentioned growth and seasonality parameters (**Table 2**). If temperature controlled the growth of

761 *R. diluvianum* shells, larger temperature seasonality would increase the chance of crossing thresholds of

762 temperature tolerance which would shorten the length of the growing season. All this suggests that

763 temperature seasonality may not have been the dominant factor causing growth cessations in *R.

764 diluvianum*. This hypothesis is supported by the observation that temperatures at which growth cessations

765 occur (16.9 ± 0.7°C; **Fig. 11a**) show large variability and do not correspond significantly to the lowest

766 temperatures of the year. A possible explanation might be that these growth cessations occurred in

767 response to attempted predation or extreme weather events, which are not necessarily paced to the

768 seasonal cycle.

769 These observations do not necessarily show that *R. diluvianum* tolerated larger temperature differences

770 than modern oyster taxa, because the extent of seasonality (14-25°C) causes neither the lower (~10°C)

771 nor the upper temperature limit (~28°C) between which shell growth occurs in modern oysters to be

772 reached. If temperature tolerance of *R. diluvianum* did resemble that of its closest modern relatives, then

773 the mild seasonal temperatures at Ivö Klack might have provided the ideal temperature range for its growth.

774 Perhaps these favorable conditions partly explain why biodiversity and abundance of invertebrates at Ivö

775 Klack was so high (Surlyk and Sørensen, 2010).

776   5.5.3 Productivity

777   Shell growth in *R. diluvianum* may not have been governed by temperature, but rather by changes in

778   productivity. The observation that peak growth rates and settling both occur during the early spring or late

779   autumn season (before or after the growth cessation; **Fig. 11b**) supports this hypothesis. Spring or autumn

780   productivity blooms caused by increases in nutrient-rich freshwater from onshore (Arthur et al., 1983; Krantz

781   et al., 1987) or due to storm-induced mixing of more nutrient-rich deeper waters are common in present-

782   day mid- and high-latitude marine ecosystems (e.g. Waniek, 2003; Danielsson et al., 2008). An increase in

783   seasonal freshwater influx would cause longer growth cessations to occur in the spring season, reducing

784   the length of the growing season while also dampening the temperature seasonality reconstructed from

785     $\delta^{18}O$ due to the influx of isotopically light fresh water which dampens the seasonal cycle (see **5.5.2**). This

786   explains the correlation found between these two parameters (**Table 2**). At the same time, this freshwater

787   input would increase reconstructed MAT by increasing $\delta^{18}O$ values in *R. diluvianum* shells, explaining the

788   weak positive correlation between MAT and length of the growing season (**Table 2**).

789   The occurrence of spring blooms is supported by weak 0.5-1.0‰ seasonal variability in $\delta^{13}C$ (**Fig. 6**).

790   Seasonal changes in productivity and/or salinity will cause changes in DIC in the environment, which are

791   apparent in the $\delta^{13}C$ of the shell above the ontogenetic trends and the effect of respiration on $\delta^{13}C$ (see **2.4**;

792   **Table 1**). The fact that a clear seasonality in $\delta^{13}C$ is absent from the stack in **Fig. 9** shows that these

793   productivity peaks do not occur at regular times of the year and that their effect on $\delta^{13}C$ is obscured by

794   ontogenetic trends. The 0.5-1.0‰ shifts in $\delta^{13}C$ that appear to be seasonal are much smaller than those in

795   modern oyster records (2-3‰ in low-latitude estuarine *Crassostrea virginica*; Surge et al., 2001; 2003;

796   Surge and Lohmann, 2008). Instead, the determined shifts more closely resemble the 0.5‰ variability in

797     $\delta^{13}C$ observed in modern *Crassostrea gigas* from the same approximate latitude as Ivö Klack in the North

798   Sea (Ullmann et al., 2013). The extreme isotopic shifts in the estuarine *C. virginica* specimens have been

799   shown to be caused by large shifts in freshwater input due to large seasonal variations in rainfall over

800   southern North America (Surge et al., 2003), while smaller variations in *C. gigas* from the North Sea are

801   produced by DIC changes due to seasonal changes in productivity (e.g. spring blooms; Ullmann et al.,

802   2013), indirect effects of temperature variability (Chauvaud et al., 2011) and changes in food source

803   (Marchais et al., 2015). The closer resemblance of *R. diluvianum* to the North Sea condition shows that the

804   Ivö Klack paleoenvironment did not experience large seasonal shifts in freshwater input and may have seen

805   productivity peaks in spring season. The latter interpretation is in agreement with the coincidence of

806   negative $\delta^{13}C$ excursions (in parts of the records not affected by ontogenetic trends and respiration) with

807   the high-$\delta^{18}O$ season (winter or spring; **Fig. 6**; **S6**), the settling of larvae and the onset of shell growth and

808   a peak in growth rates in the spring season (much like in wild modern oysters; Berthelin et al., 2000; **Fig.**

809   **9**; **Fig. 11a**).

810

811   5.5.4 Ontogeny

812   A part of the variation in $\delta^{13}C$ is explained by the presence of ontogenetic trends. These trends are known

813   to occur in marine and freshwater bivalves including in bivalves with symbionts (Klein et al., 1996b;

814   Watanabe et al., 2004; Gillikin et al., 2007; McConnaughey and Gillikin, 2008). The scale and direction of

815   the trends in $\delta^{13}C$ are not consistent between individual *R. diluvianum* shells, which is also the case in other

816   bivalve species (see **section 4.5**; **Table 1**; McConnaughey and Gillikin, 2008 and references therein).

817   Studies of modern bivalves show that in larger (older) bivalves, the contribution of respired CO_2 to carbon

818   in the shell is larger (up to 40%; Gillikin et al., 2007). This finding explains common trends of reducing $\delta^{13}C$

819   with age in bivalve shells, since respired carbon is isotopically lighter than environmental DIC. Since

820   ontogenetic trends are likely caused by changes in the amount of respired carbon entering the shell, but

821   the direction of these trends is inconsistent in *R. diluvianum*, the contribution of respired CO_2 to *R.*

822   *diluvianum* shells likely did not strictly increase with age. While this complicates the interpretation of $\delta^{13}C$

823   records, the relative contribution of environmental changes to $\delta^{13}C$ variability in *R. diluvianum* shells does

824   appear to be highest at the positive end of the ontogenetic trend.

825

826   **5. Conclusions**

827   The highly biodiverse marine invertebrate community at Ivö Klack in the Kristianstad Basin in southern

828   Sweden offers a unique opportunity to recover a wealth of information about Campanian climate and

829　environment in high latitudes and the ecology and life of extinct invertebrate species that lived under these

830　conditions. The lack of burial and tectonic activity in the region favored *Rastellum diluvianum* fossil shells

831　from Ivö Klack to be well preserved, as is evident from the excellent preservation of growth structures typical

832　for ostreid shells as well as from the limited evidence for geochemical changes associated with diagenetic

833　alteration. This excellent preservation allows the shells of *R. diluvianum* to be used to accurately and

834　precisely constrain the age of the Ivö Klack locality using strontium isotope stratigraphy (78.14 ± 0.26 Ma;

835　$^{87}Sr/^{86}Sr$ = 0.707552 ± 0.000112). Furthermore, *R. diluvianum* shells reveal sub-annual scale variability in

836　temperature, local environment and growth rates through a multi-proxy geochemical approach. The

837　combination of trace element and stable isotope measurements with growth modelling based on $\delta^{18}O$

838　records in the shells allow all measured proxies to be aligned on the same time axis. Application of transfer

839　functions for potential Mg/Ca, Mg/Li and Sr/Li temperature proxies established in modern invertebrates

840　yields temperatures consistent with those calculated from $\delta^{18}O$ records. However, close examination of the

841　seasonal phase relationships between these proxies reveals that the sub-annual variability in these trace

842　element ratios is not controlled by temperature changes alone. This observation supports previous studies

843　that found the expression of trace element proxies to be highly variable among species and even among

844　different specimens of the same species. If trace element proxies are to be used for seasonality

845　reconstructions in pre-Quaternary times, a more robust, non-species-specific model for the incorporation of

846　trace elements by bivalves is required. Establishing such a model requires culture experiments with different

847　bivalve species in which multiple parameters influencing trace element composition can be controlled (e.g.

848　temperature, salinity, food intake and microstructure).

849　Stable isotope records in *R. diluvianum* shells reveal a MAT of 19°C with a seasonal water temperature

850　range of ±11°C (14-25°C) at Ivö Klack. This value for MAT is lower than full marine SST of Boreal Chalk

851　recently reevaluated with the clumped isotope thermometer. The difference highlights potential biases in

852　temperature reconstructions based on $\delta^{18}O$ values and argues for reevaluations of these proxy records

853　with more accurate techniques such as clumped isotope analysis. Comparing the seasonal temperature

854　range reconstructed from *R. diluvianum* shells with other Late Cretaceous seasonality records from lower

855　latitudes reveals that both latitudinal gradients and SST seasonality outside the tropics were much higher

856　than predicted by climate models. This disagreement between data and models clearly illustrates the need

857   for more data on Late Cretaceous seasonality outside the (sub-)tropical latitudes and highlights how

858   important such proxy-based reconstructions are for improving our understanding of the dynamics in

859   temperature variability in both space and time during greenhouse climates.

860   Finally, the coupled modelling and multi-proxy approach applied in this study sheds light on the effects of

861   environmental changes on the life cycle and sub-annual growth of *R. diluvianum* shells. This study reveals

862   that growth curves of *R. diluvianum* strongly resemble those in modern shallow marine bivalves that grow

863   in coastal high latitude environments. However, ontogenetic changes in growth rate of our Boreal oysters

864   seem unrelated to temperature, in contrast to modern, high-latitude oysters that tend to lower their growth

865   rate and cease mineralization below a certain cold threshold. We conclude that growth cessations and sub-

866   annual changes in growth rate in *R. diluvianum* were most likely not caused by intolerable temperatures,

867   but rather by circadian rhythm tied to the seasonal cycle and seasonal changes in sea surface productivity,

868   driven by nutrient-rich freshwater inputs.

869

883   shells and Roger Barlow for his assistance in handling strontium isotope measurements with asymmetric

884   error distributions.

885

886 **Supplementary files**

887 All supplementary files are stored in the open access online database Zenodo and can be accessed using

888 the following link: https://doi.org/10.5281/zenodo.3699542

889

890 **S1**: High resolution (6400 dpi) scans of cross sections through the 12 shells of *Rastellum diluvianum* used

891 in this study.

892 **S2**: Compilation of µXRF maps of cross sections through the 12 shells of *Rastellum diluvianum* used in this

893 study.

894 **S3**: Compilation of XRF line scans measured through the foliated calcite of *Rastellum diluvianum* shells.

895 **S4**: Compilation of LA-ICP-MS data collected within the context of this study.

896 **S5**: Compilation of IRMS data used in this study.

897 **S6**: Composite figures of XRF linescan data through the shells of *Rastellum diluvianum*.

898 **S7**: Source code of the bivalve growth model adapted from Judd et al. (2018) including temperature

899 equations for calcite.

900 **S8**: Compilation of strontium isotope data and ages used in this study.

901 **S9**: Compilation of the results from growth modelling on 5 *Rastellum diluvianum* shells.

902 **S10**: Compilation figures of proxy record data plotted on time axis for all 5 shells for which modelling was

903 carried out.

904 **S11**: Plot of ontogenetic trends in $\delta^{13}C$ and Li/Ca proxies including statistics on the spread of the slopes of

905 these trends.

906 **S12**: Data on trends in $\delta^{13}C$ and Li/Ca.

907 **S13**: Data used to create seasonality crossplots shown in **Fig. 7**.

908 **S14**: Data on statistics of the growth rates, seasonality and spawning season of all 5 bivalves for which

909 modelling was done.

910

911 **References**

912 Al-Aasm, I. S. and Veizer, J.: Diagenetic stabilization of aragonite and low-Mg calcite, II. Stable isotopes in rudists, Journal of
913 Sedimentary Research, 56(6), 763–770, 1986a.

914 Al-Aasm, I. S. and Veizer, J.: Diagenetic stabilization of aragonite and low-Mg calcite, I. Trace elements in rudists, Journal of
915   Sedimentary Research, 56(1), 138–152, 1986.
916 Alberti, M., Fürsich, F. T., Abdelhady, A. A. and Andersen, N.: Middle to Late Jurassic equatorial seawater temperatures and
917   latitudinal temperature gradients based on stable isotopes of brachiopods and oysters from Gebel Maghara, Egypt,
918   Palaeogeography, Palaeoclimatology, Palaeoecology, 468, 301–313, doi:10.1016/j.palaeo.2016.11.052, 2017.
919 Amiot, R., Lécuyer, C., Buffetaut, E., Fluteau, F., Legendre, S. and Martineau, F.: Latitudinal temperature gradient during the
920   Cretaceous Upper Campanian–Middle Maastrichtian: δ18O record of continental vertebrates, Earth and Planetary Science
921   Letters, 226(1), 255–272, doi:10.1016/j.epsl.2004.07.015, 2004.
922 Andreasson, F. P. and Schmitz, B.: Winter and summer temperatures of the early middle Eocene of France from Turritella ☐18O
923   profiles, , 4, 1996.
924 Arthur, M. A., Williams, D. F. and Jones, D. S.: Seasonal temperature-salinity changes and thermocline development in the mid-
925   Atlantic Bight as recorded by the isotopic composition of bivalves, Geology, 11(11), 655–659, doi:10.1130/0091-
926   7613(1983)11<655:STCATD>2.0.CO;2, 1983.
927 Bachelet, G.: Growth and recruitment of the tellinid bivalve Macoma balthica at the southern limit of its geographical distribution, the
928   Gironde estuary (SW France), Marine Biology, 59(2), 105–117, 1980.
929 Barlow, R.: Asymmetric systematic errors, arXiv preprint physics/0306138, 2003.
930 Barrera, E. and Johnson, C. C.: Evolution of the Cretaceous Ocean-climate System, Geological Society of America., 1999.
931 Berthelin, C., Kellner, K. and Mathieu, M.: Storage metabolism in the Pacific oyster (Crassostrea gigas) in relation to summer
932   mortalities and reproductive cycle (West Coast of France), Comparative Biochemistry and Physiology Part B: Biochemistry and
933   Molecular Biology, 125(3), 359–369, doi:10.1016/S0305-0491(99)00187-X, 2000.
934 Brand, U. and Veizer, J.: Chemical diagenesis of a multicomponent carbonate system–1: Trace elements, Journal of Sedimentary
935   Research, 50(4), 1219–1236, 1980.
936 Brand, U. and Veizer, J.: Chemical diagenesis of a multicomponent carbonate system-2: stable isotopes, Journal of Sedimentary
937   Research, 51(3), 987–997, 1981.
938 Bryan, S. P. and Marchitto, T. M.: Mg/Ca–temperature proxy in benthic foraminifera: New calibrations from the Florida Straits and a
939   hypothesis regarding Mg/Li, Paleoceanography, 23(2), PA2220, doi:10.1029/2007PA001553, 2008.
940 Burgener, L., Hyland, E., Huntington, K. W., Kelson, J. R. and Sewall, J. O.: Revisiting the equable climate problem during the Late
941   Cretaceous greenhouse using paleosol carbonate clumped isotope temperatures from the Campanian of the Western Interior
942   Basin, USA, Palaeogeography, Palaeoclimatology, Palaeoecology, 516, 244–267, doi:10.1016/j.palaeo.2018.12.004, 2018.
943 Butler, P. G., Wanamaker, A. D., Scourse, J. D., Richardson, C. A. and Reynolds, D. J.: Variability of marine climate on the North
944   Icelandic Shelf in a 1357-year proxy archive based on growth increments in the bivalve Arctica islandica, Palaeogeography,
945   Palaeoclimatology, Palaeoecology, 373, 141–151, doi:10.1016/j.palaeo.2012.01.016, 2013.
946 Carriker, M. R., Palmer, R. E. and Prezant, R. S.: Functional ultramorphology of the dissoconch valves of the oyster Crassostrea
947   virginica, in Proceedings of the National Shellfisheries Association, vol. 70, pp. 139–183. [online] Available from:
948   https://www.researchgate.net/profile/Robert_Prezant2/publication/236964411_Functional_ultramorphology_of_the_dissoconch_
949   valves_of_the_oyster_Crassostrea_virginica/links/53dfd2260cf2a768e49be892.pdf, 1979.
950 Carriker, M. R., Swann, C. P., Prezant, R. S. and Counts, C. L.: Chemical elements in the aragonitic and calcitic microstructural
951   groups of shell of the oysterCrassostrea virginica: A proton probe study, Marine Biology, 109(2), 287–297, 1991.
952 Chauvaud, L., Thébault, J., Clavier, J., Lorrain, A. and Strand, Ø.: What's Hiding Behind Ontogenetic δ13C Variations in Mollusk
953   Shells? New Insights from the Great Scallop (Pecten maximus), Estuaries and Coasts, 34(2), 211–220, doi:10.1007/s12237-
954   010-9267-4, 2011.
955 Christensen, W. K.: Upper Cretaceous belemnites from the Kristianstad area in Scania, Fossils and Strata., 1975.
956 Christensen, W. K.: The Albian to Maastrichtian of southern Sweden and Bornholm, Denmark: a review, Cretaceous Research, 5(4),
957   313–327, 1984.
958 Christensen, W. K.: Paleobiogeography and migration in the Late Cretaceous belemnite family Belemnitellidae, Acta
959   palaeontologica polonica, 42(4), 457–495, 1997.
960 Clarke, L. J. and Jenkyns, H. C.: New oxygen isotope evidence for long-term Cretaceous climatic change in the Southern
961   Hemisphere, Geology, 27(8), 699–702, 1999.
962 Cochran, J. K., Kallenberg, K., Landman, N. H., Harries, P. J., Weinreb, D., Turekian, K. K., Beck, A. J. and Cobban, W. A.: Effect of
963   diagenesis on the Sr, O, and C isotope composition of late Cretaceous mollusks from the Western Interior Seaway of North
964   America, American Journal of Science, 310(2), 69–88, doi:10.2475/02.2010.01, 2010.
965 Coggon, R. M., Teagle, D. A., Smith-Duque, C. E., Alt, J. C. and Cooper, M. J.: Reconstructing past seawater Mg/Ca and Sr/Ca
966   from mid-ocean ridge flank calcium carbonate veins, Science, 327(5969), 1114–1117, 2010.
967 Cognie, B., Haure, J. and Barillé, L.: Spatial distribution in a temperate coastal ecosystem of the wild stock of the farmed oyster
968   Crassostrea gigas (Thunberg), Aquaculture, 259(1–4), 249–259, 2006.
969 Csiki-Sava, Z., Buffetaut, E., Ősi, A., Pereda-Suberbiola, X. and Brusatte, S. L.: Island life in the Cretaceous - faunal composition,
970   biogeography, evolution, and extinction of land-living vertebrates on the Late Cretaceous European archipelago, Zookeys,
971   (469), 1–161, doi:10.3897/zookeys.469.8439, 2015.
972 Dalbeck, P., England, J., Cusack, M., Lee, M. R. and Fallick, A. E.: Crystallography and chemistry of the calcium carbonate
973   polymorph switch in M. edulis shells, European Journal of Mineralogy, 18(5), 601–609, doi:10.1127/0935-1221/2006/0018-0601,
974   2006.
975 Danielsson, \AAsa, Papush, L. and Rahm, L.: Alterations in nutrient limitations—scenarios of a changing Baltic Sea, Journal of
976   Marine Systems, 73(3–4), 263–283, 2008.
977 De Villiers, S.: Seawater strontium and Sr/Ca variability in the Atlantic and Pacific oceans, Earth and Planetary Science Letters,
978   171(4), 623–634, 1999.
979 DeConto, R. M., Hay, W. W., Thompson, S. L. and Bergengren, J.: Late Cretaceous climate and vegetation interactions: cold
980   continental interior paradox, SPECIAL PAPERS-GEOLOGICAL SOCIETY OF AMERICA, 391–406, 1999.
981 Dellinger, M., West, A. J., Paris, G., Adkins, J. F., von Strandmann, P. A. P., Ullmann, C. V., Eagle, R. A., Freitas, P., Bagard, M.-L.
982   and Ries, J. B.: The Li isotope composition of marine biogenic carbonates: Patterns and Mechanisms, Geochimica et
983   Cosmochimica Acta, 236, 315–335, 2018.

47

984   Donnadieu, Y., Pucéat, E., Moiroud, M., Guillocheau, F. and Deconinck, J.-F.: A better-ventilated ocean triggered by Late
985   Cretaceous changes in continental configuration, Nature Communications, 7, 10316, doi:10.1038/ncomms10316, 2016.
986   El Meknassi, S., Dera, G., Cardone, T., De Rafélis, M., Brahmi, C. and Chavagnac, V.: Sr isotope ratios of modern carbonate shells:
987   Good and bad news for chemostratigraphy, Geology, 46(11), 1003–1006, 2018.
988   Fan, C., Koeniger, P., Wang, H. and Frechen, M.: Ligamental increments of the mid-Holocene Pacific oyster Crassostrea gigas are
989   reliable independent proxies for seasonality in the western Bohai Sea, China, Palaeogeography, palaeoclimatology,
990   palaeoecology, 299(3–4), 437–448, 2011.
991   Freitas, P. S., Clarke, L. J., Kennedy, H. A. and Richardson, C. A.: Inter-and intra-specimen variability masks reliable temperature
992   control on shell Mg/Ca ratios in laboratory and field cultured Mytilus edulis and Pecten maximus (bivalvia), Biogeosciences
993   Discussions, 5(1), 531–572, 2008.
994   Friedrich, O., Herrle, J. O. and Hemleben, C.: Climatic changes in the late Campanian—early Maastrichtian: Micropaleontological
995   and stable isotopic evidence from an epicontinental sea, Journal of Foraminiferal Research, 35(3), 228–247, 2005.
996   Friedrich, O., Herrle, J. O., Wilson, P. A., Cooper, M. J., Erbacher, J. and Hemleben, C.: Early Maastrichtian carbon cycle
997   perturbation and cooling event: Implications from the South Atlantic Ocean, Paleoceanography, 24(2), PA2211,
998   doi:10.1029/2008PA001654, 2009.
999   Friedrich, O., Norris, R. D. and Erbacher, J.: Evolution of middle to Late Cretaceous oceans—a 55 my record of Earth's temperature
1000   and carbon cycle, Geology, 40(2), 107–110, 2012.
1001   Füllenbach, C. S., Schöne, B. R. and Mertz-Kraus, R.: Strontium/lithium ratio in aragonitic shells of Cerastoderma edule (Bivalvia)—
1002   A new potential temperature proxy for brackish environments, Chemical Geology, 417, 341–355, 2015.
1003   Galtsoff, P. S.: The American Oyster: US Fish and Wildlife Service, Fishery Bulletin, 64, 480, 1964.
1004   Gillikin, D. P., Lorrain, A., Navez, J., Taylor, J. W., André, L., Keppens, E., Baeyens, W. and Dehairs, F.: Strong biological controls
1005   on Sr/Ca ratios in aragonitic marine bivalve shells, Geochemistry, Geophysics, Geosystems, 6(5), Q05009, 2005.
1006   Gillikin, D. P., Lorrain, A., Bouillon, S., Willenz, P. and Dehairs, F.: Stable carbon isotopic composition of Mytilus edulis shells:
1007   relation to metabolism, salinity, δ 13 C DIC and phytoplankton, Organic Geochemistry, 37(10), 1371–1382, 2006.
1008   Gillikin, D. P., Lorrain, A., Meng, L. and Dehairs, F.: A large metabolic carbon contribution to the δ 13 C record in marine aragonitic
1009   bivalve shells, Geochimica et Cosmochimica Acta, 71(12), 2936–2946, 2007.
1010   Hart, D. R. and Chute, A. S.: Verification of Atlantic sea scallop (Placopecten magellanicus) shell growth rings by tracking cohorts in
1011   fishery closed areas, Canadian Journal of Fisheries and Aquatic Sciences, 66(5), 751–758, 2009.
1012   Hay, W. W. and Floegel, S.: New thoughts about the Cretaceous climate and oceans, Earth-Science Reviews, 115(4), 262–272,
1013   2012.
1014   van Hinsbergen, D. J., de Groot, L. V., van Schaik, S. J., Spakman, W., Bijl, P. K., Sluijs, A., Langereis, C. G. and Brinkhuis, H.: A
1015   paleolatitude calculator for paleoclimate studies, PloS one, 10(6), e0126946, 2015.
1016   Högdahl, K., Andersson, U. B. and Eklund, O.: The Transscandinavian Igneous Belt (TIB) in Sweden: a review of its character and
1017   evolution, Geological survey of Finland Espoo., 2004.
1018   Huber, B. T., Norris, R. D. and MacLeod, K. G.: Deep-sea paleotemperature record of extreme warmth during the Cretaceous,
1019   Geology, 30(2), 123–126, 2002.
1020   Huck, S., Heimhofer, U., Rameil, N., Bodin, S. and Immenhauser, A.: Strontium and carbon-isotope chronostratigraphy of
1021   Barremian–Aptian shoal-water carbonates: Northern Tethyan platform drowning predates OAE 1a, Earth and Planetary Science
1022   Letters, 304(3–4), 547–558, doi:10.1016/j.epsl.2011.02.031, 2011.
1023   Huyghe, D., Lartaud, F., Emmanuel, L., Merle, D. and Renard, M.: Palaeogene climate evolution in the Paris Basin from oxygen
1024   stable isotope (δ18O) compositions of marine molluscs, Journal of the Geological Society, 172(5), 576–587, 2015.
1025   Huyghe, D., de Rafelis, M., Ropert, M., Mouchi, V., Emmanuel, L., Renard, M. and Lartaud, F.: New insights into oyster high-
1026   resolution hinge growth patterns, Mar Biol, 166(4), 48, doi:10.1007/s00227-019-3496-2, 2019.
1027   Immenhauser, A., Nägler, T. F., Steuber, T. and Hippler, D.: A critical assessment of mollusk 18 O/16 O, Mg/Ca, and 44 Ca/40 Ca
1028   ratios as proxies for Cretaceous seawater temperature seasonality, Palaeogeography, Palaeoclimatology, Palaeoecology,
1029   215(3), 221–237, 2005.
1030   IPCC: IPCC, 2013: Climate Change 2013: The Physical Science Basis. Contribution of Working Group I to the Fifth Assessment
1031   Report of the Intergovernmental Panel on Climate Change, 1535 pp, Cambridge Univ. Press, Cambridge, UK, and New York.,
1032   2013.
1033   IRI/LDEO Climate Data Library URL http://iridl.ldeo.columbia.edu (accessed 06/03/20).
1034   Ivany, L. C.: Reconstructing paleoseasonality from accretionary skeletal carbonates—challenges and opportunities, The
1035   Paleontological Society Papers, 18, 133–166, 2012.
1036   Ivany, L. C. and Runnegar, B.: Early Permian seasonality from bivalve δ18O and implications for the oxygen isotopic composition of
1037   seawater, Geology, 38(11), 1027–1030, 2010.
1038   Jablonski, D., Huang, S., Roy, K. and Valentine, J. W.: Shaping the latitudinal diversity gradient: new perspectives from a synthesis
1039   of paleobiology and biogeography, The American Naturalist, 189(1), 1–12, 2017.
1040   Jarvis, I., Mabrouk, A., Moody, R. T. and de Cabrera, S.: Late Cretaceous (Campanian) carbon isotope events, sea-level change
1041   and correlation of the Tethyan and Boreal realms, Palaeogeography, Palaeoclimatology, Palaeoecology, 188(3), 215–248,
1042   2002.
1043   Jenkyns, H. C., Gale, A. S. and Corfield, R. M.: Carbon-and oxygen-isotope stratigraphy of the English Chalk and Italian Scaglia and
1044   its palaeoclimatic significance, Geological Magazine, 131(1), 1–34, 1994.
1045   Jenkyns, H. C., Forster, A., Schouten, S. and Damsté, J. S. S.: High temperatures in the late Cretaceous Arctic Ocean, Nature,
1046   432(7019), 888, 2004.
1047   Jones, D. S.: Sclerochronology: reading the record of the molluscan shell: annual growth increments in the shells of bivalve
1048   molluscs record marine climatic changes and reveal surprising longevity, American Scientist, 71(4), 384–391, 1983.
1049   Judd, E. J., Wilkinson, B. H. and Ivany, L. C.: The life and time of clams: Derivation of intra-annual growth rates from high-resolution
1050   oxygen isotope profiles, Palaeogeography, Palaeoclimatology, Palaeoecology, 490, 70–83, 2018.
1051   Kawaguchi, T. and Watabe, N.: The organic matrices of the shell of the American oyster Crassostrea virginica Gmelin, Journal of
1052   Experimental Marine Biology and Ecology, 170(1), 11–28, doi:10.1016/0022-0981(93)90126-9, 1993.

Kim, S.-T. and O'Neil, J. R.: Equilibrium and nonequilibrium oxygen isotope effects in synthetic carbonates, Geochimica et Cosmochimica Acta, 61(16), 3461–3475, 1997.

Klein, R. T., Lohmann, K. C. and Thayer, C. W.: Bivalve skeletons record sea-surface temperature and δ18O via Mg/Ca and 18O/16O ratios, Geology, 24(5), 415–418, 1996a.

Klein, R. T., Lohmann, K. C. and Thayer, C. W.: SrCa and 13C12C ratios in skeletal calcite of Mytilus trossulus: Covariation with metabolic rate, salinity, and carbon isotopic composition of seawater, Geochimica et Cosmochimica Acta, 60(21), 4207–4221, doi:10.1016/S0016-7037(96)00232-3, 1996b.

Kominz, M. A., Browning, J. V., Miller, K. G., Sugarman, P. J., Mizintseva, S. and Scotese, C. R.: Late Cretaceous to Miocene sea-level estimates from the New Jersey and Delaware coastal plain coreholes: an error analysis, Basin Research, 20(2), 211–226, 2008.

Krantz, D. E., Williams, D. F. and Jones, D. S.: Ecological and paleoenvironmental information using stable isotope profiles from living and fossil molluscs, Palaeogeography, Palaeoclimatology, Palaeoecology, 58(3), 249–266, doi:10.1016/0031-0182(87)90064-2, 1987.

Kuznetsov, A. B., Semikhatov, M. A. and Gorokhov, I. M.: The Sr isotope composition of the world ocean, marginal and inland seas: Implications for the Sr isotope stratigraphy, Stratigr. Geol. Correl., 20(6), 501–515, doi:10.1134/S0869593812060044, 2012.

Lartaud, F., Emmanuel, L., De Rafélis, M., Ropert, M., Labourdette, N., Richardson, C. A. and Renard, M.: A latitudinal gradient of seasonal temperature variation recorded in oyster shells from the coastal waters of France and The Netherlands, Facies, 56(1), 13, 2010.

Lear, C. H., Elderfield, H. and Wilson, P. A.: A Cenozoic seawater Sr/Ca record from benthic foraminiferal calcite and its application in determining global weathering fluxes, Earth and Planetary Science Letters, 208(1), 69–84, doi:10.1016/S0012-821X(02)01156-1, 2003.

Li, Y., Qin, J. G., Abbott, C. A., Li, X. and Benkendorff, K.: Synergistic impacts of heat shock and spawning on the physiology and immune health of Crassostrea gigas: an explanation for summer mortality in Pacific oysters, American Journal of Physiology-Regulatory, Integrative and Comparative Physiology, 293(6), R2353–R2362, 2007.

Locarnini, R. A., Mishonov, A. V., Antonov, J. I., Boyer, T. P., Garcia, H. E., Baranova, O. K., Zweng, M. M., Paver, C. R., Reagan, J. R., Johnson, D. R., Hamilton, M. and Seidov, D.: World ocean atlas 2013. Volume 1, Temperature, U.S. Department of Commerce, National Oceanic and Atmospheric Administration, National Environmental Satellite, Data and Information Service, doi:10.7289/v55x26vd, 2013.

Lorrain, A., Paulet, Y.-M., Chauvaud, L., Dunbar, R., Mucciarone, D. and Fontugne, M.: δ 13 C variation in scallop shells: increasing metabolic carbon contribution with body size?, Geochimica et Cosmochimica Acta, 68(17), 3509–3519, 2004.

Lorrain, A., Gillikin, D. P., Paulet, Y.-M., Chauvaud, L., Le Mercier, A., Navez, J. and André, L.: Strong kinetic effects on Sr/Ca ratios in the calcitic bivalve Pecten maximus, Geology, 33(12), 965–968, 2005.

Lowenstam, H. A. and Epstein, S.: Paleotemperatures of the post-Aptian Cretaceous as determined by the oxygen isotope method, The Journal of Geology, 62(3), 207–248, 1954.

MacDonald, B. A. and Thompson, R. J.: Influence of temperature and food availability on the ecological energetics of the giant scallop Placopecten magellanicus. I. Growth rates of shell and somatic tissue., Marine ecology progress series. Oldendorf, 25(3), 279–294, 1985.

Marchais, V., Richard, J., Jolivet, A., Flye-Sainte-Marie, J., Thébault, J., Jean, F., Richard, P., Paulet, Y.-M., Clavier, J. and Chauvaud, L.: Coupling experimental and field-based approaches to decipher carbon sources in the shell of the great scallop, Pecten maximus (L.), Geochimica et Cosmochimica Acta, 168, 58–69, doi:10.1016/j.gca.2015.07.010, 2015.

McArthur, J. M., Howarth, R. J. and Bailey, T. R.: Strontium Isotope Stratigraphy: LOWESS Version 3: Best Fit to the Marine Sr-Isotope Curve for 0–509 Ma and Accompanying Look-up Table for Deriving Numerical Age, The Journal of Geology, 109(2), 155–170, doi:10.1086/319243, 2001.

McArthur, J. M., Steuber, T., Page, K. N. and Landman, N. H.: Sr-isotope stratigraphy: assigning time in the Campanian, Pliensbachian, Toarcian, and Valanginian, The Journal of Geology, 124(5), 569–586, 2016.

McConnaughey, T. A.: Sub-equilibrium oxygen-18 and carbon-13 levels in biological carbonates: carbonate and kinetic models, Coral Reefs, 22(4), 316–327, 2003.

McConnaughey, T. A. and Gillikin, D. P.: Carbon isotopes in mollusk shell carbonates, Geo-Marine Letters, 28(5–6), 287–299, doi:10.1007/s00367-008-0116-4, 2008.

McConnaughey, T. A., Burdett, J., Whelan, J. F. and Paull, C. K.: Carbon isotopes in biological carbonates: respiration and photosynthesis, Geochimica et Cosmochimica Acta, 61(3), 611–622, 1997.

Meyers, S. R. and Malinverno, A.: Proterozoic Milankovitch cycles and the history of the solar system, PNAS, 201717689, doi:10.1073/pnas.1717689115, 2018.

Miller, K. G., Wright, J. D. and Browning, J. V.: Visions of ice sheets in a greenhouse world, Marine Geology, 217(3), 215–231, doi:10.1016/j.margeo.2005.02.007, 2005.

Montgomery, P., Hailwood, E. A., Gale, A. S. and Burnett, J. A.: The magnetostratigraphy of Coniacian-Late Campanian chalk sequences in southern England, Earth and Planetary Science Letters, 156(3), 209–224, doi:10.1016/S0012-821X(98)00008-9, 1998.

Mook, W. G.: Paleotemperatures and chlorinities from stable carbon and oxygen isotopes in shell carbonate, Palaeogeography, Palaeoclimatology, Palaeoecology, 9(4), 245–263, doi:10.1016/0031-0182(71)90002-2, 1971.

Mouchi, V., De Rafélis, M., Lartaud, F., Fialin, M. and Verrecchia, E.: Chemical labelling of oyster shells used for time-calibrated high-resolution Mg/Ca ratios: a tool for estimation of past seasonal temperature variations, Palaeogeography, Palaeoclimatology, Palaeoecology, 373, 66–74, 2013.

NOAA Earth System Research Laboratory: NOAA Optimum Interpolation (IO) Sea Surface Temperature (SST) http://www.esrl.noaa.gov/psd/data/gridded/data.noaa.oisst.v2.html (accessed 01/21/19).

O'Brien, C. L., Robinson, S. A., Pancost, R. D., Sinninghe Damsté, J. S., Schouten, S., Lunt, D. J., Alsenz, H., Bornemann, A., Bottini, C., Brassell, S. C., Farnsworth, A., Forster, A., Huber, B. T., Inglis, G. N., Jenkyns, H. C., Linnert, C., Littler, K., Markwick, P., McAnena, A., Mutterlose, J., Naafs, B. D. A., Püttmann, W., Sluijs, A., van Helmond, N. A. G. M., Vellekoop, J., Wagner, T. and Wrobel, N. E.: Cretaceous sea-surface temperature evolution: Constraints from TEX 86 and planktonic foraminiferal oxygen isotopes, Earth-Science Reviews, 172, 224–247, doi:10.1016/j.earscirev.2017.07.012, 2017.

1123   Ogg, J. G., Ogg, G. and Gradstein, F. M.: A concise geologic time scale: 2016, Elsevier., 2016.
1124   Palmer, R. E. and Carriker, M. R.: Effects of cultural conditions on morphology of the shell of the oyster Crassostrea virginica, in
1125   Proceedings of the National Shellfisheries Association, vol. 69, pp. 58–72., 1979.
1126   Pearson, P. N., Ditchfield, P. W., Singano, J., Harcourt-Brown, K. G., Nicholas, C. J., Olsson, R. K., Shackleton, N. J. and Hall, M.
1127   A.: Warm tropical sea surface temperatures in the Late Cretaceous and Eocene epochs, Nature, 413(6855), 481, 2001.
1128   Perdiou, A., Thibault, N., Anderskouv, K., Van Buchem, F., Buijs, G. J. A. and Bjerrum, C. J.: Orbital calibration of the late
1129   Campanian carbon isotope event in the North Sea, Journal of the Geological Society, 173(3), 504–517, 2016.
1130   Prandle, D. and Lane, A.: The annual temperature cycle in shelf seas, Continental Shelf Research, 15(6), 681–704,
1131   doi:10.1016/0278-4343(94)E0029-L, 1995.
1132   Rausch, S., Böhm, F., Bach, W., Klügel, A. and Eisenhauer, A.: Calcium carbonate veins in ocean crust record a threefold increase
1133   of seawater Mg/Ca in the past 30 million years, Earth and Planetary Science Letters, 362, 215–224, 2013.
1134   Rayner, N. A., Parker, D. E., Horton, E. B., Folland, C. K., Alexander, L. V., Rowell, D. P., Kent, E. C. and Kaplan, A.: Global
1135   analyses of sea surface temperature, sea ice, and night marine air temperature since the late nineteenth century, Journal of
1136   Geophysical Research: Atmospheres, 108(D14), doi:10.1029/2002JD002670, 2003.
1137   Reid, R. E. H.: The Chalk Sea, The Irish Naturalists' Journal, 17(11), 357–375, 1973.
1138   Richardson, C. A., Peharda, M., Kennedy, H., Kennedy, P. and Onofri, V.: Age, growth rate and season of recruitment of Pinna
1139   nobilis (L) in the Croatian Adriatic determined from Mg: Ca and Sr: Ca shell profiles, Journal of Experimental Marine Biology and
1140   Ecology, 299(1), 1–16, 2004.
1141   Roy, K., Jablonski, D. and Martien, K. K.: Invariant size–frequency distributions along a latitudinal gradient in marine bivalves,
1142   PNAS, 97(24), 13150–13155, doi:10.1073/pnas.97.24.13150, 2000.
1143   Rucker, J. B. and Valentine, J. W.: Salinity Response of Trace Element Concentration in Crassostrea virginica, Nature, 190(4781),
1144   1099–1100, doi:10.1038/1901099a0, 1961.
1145   Sano, Y., Kobayashi, S., Shirai, K., Takahata, N., Matsumoto, K., Watanabe, T., Sowa, K. and Iwai, K.: Past daily light cycle
1146   recorded in the strontium/calcium ratios of giant clam shells, Nat Commun, 3, 761, doi:10.1038/ncomms1763, 2012.
1147   Schöne, B. R. and Gillikin, D. P.: Unraveling environmental histories from skeletal diaries — Advances in sclerochronology,
1148   Palaeogeography, Palaeoclimatology, Palaeoecology, 373, 1–5, doi:10.1016/j.palaeo.2012.11.026, 2013.
1149   SCHÖNE, B. R., Houk, S. D., FREYRE CASTRO, A. D., Fiebig, J., Oschmann, W., KRÖNCKE, I., Dreyer, W. and Gosselck, F.:
1150   Daily growth rates in shells of Arctica islandica: assessing sub-seasonal environmental controls on a long-lived bivalve mollusk,
1151   Palaios, 20(1), 78–92, 2005.
1152   Schöne, B. R., Zhang, Z., Jacob, D., Gillikin, D. P., Tütken, T., Garbe-Schönberg, D., McConnaughey, T. and Soldati, A.: Effect of
1153   organic matrices on the determination of the trace element chemistry (Mg, Sr, Mg/Ca, Sr/Ca) of aragonitic bivalve shells (Arctica
1154   islandica)—Comparison of ICP-OES and LA-ICP-MS data, Geochemical Journal, 44(1), 23–37, 2010.
1155   Schöne, B. R., Zhang, Z., Radermacher, P., Thébault, J., Jacob, D. E., Nunn, E. V. and Maurer, A.-F.: Sr/Ca and Mg/Ca ratios of
1156   ontogenetically old, long-lived bivalve shells (Arctica islandica) and their function as paleotemperature proxies,
1157   Palaeogeography, Palaeoclimatology, Palaeoecology, 302(1), 52–64, 2011.
1158   Schöne, B. R., Radermacher, P., Zhang, Z. and Jacob, D. E.: Crystal fabrics and element impurities (Sr/Ca, Mg/Ca, and Ba/Ca) in
1159   shells of Arctica islandica—Implications for paleoclimate reconstructions, Palaeogeography, Palaeoclimatology, Palaeoecology,
1160   373, 50–59, 2013.
1161   Scotese, C.: A NEW GLOBAL TEMPERATURE CURVE FOR THE PHANEROZOIC., 2016.
1162   Shackleton, N. J.: Paleogene stable isotope events, Palaeogeography, Palaeoclimatology, Palaeoecology, 57(1), 91–102, 1986.
1163   Snoeck, C., Lee-Thorp, J., Schulting, R., Jong, J., Debouge, W. and Mattielli, N.: Calcined bone provides a reliable substrate for
1164   strontium isotope ratios as shown by an enrichment experiment, Rapid communications in mass spectrometry, 29(1), 107–114,
1165   2015.
1166   Sørensen, A. M., Surlyk, F. and Jagt, J. W. M.: Adaptive morphologies and guild structure in a high-diversity bivalve fauna from an
1167   early Campanian rocky shore, Ivö Klack (Sweden), Cretaceous Research, 33(1), 21–41, doi:10.1016/j.cretres.2011.07.004,
1168   2012.
1169   Sørensen, A. M., Ullmann, C. V., Thibault, N. and Korte, C.: Geochemical signatures of the early Campanian belemnite
1170   Belemnellocamax mammillatus from the Kristianstad Basin in Scania, Sweden, Palaeogeography, palaeoclimatology,
1171   palaeoecology, 433, 191–200, 2015.
1172   Stanley, S. M. and Hardie, L. A.: Secular oscillations in the carbonate mineralogy of reef-building and sediment-producing
1173   organisms driven by tectonically forced shifts in seawater chemistry, Palaeogeography, Palaeoclimatology, Palaeoecology,
1174   144(1), 3–19, 1998.
1175   Stenzel, H. B.: Aragonite and calcite as constituents of adult oyster shells, Science, 142(3589), 232–233, 1963.
1176   Steuber, T.: Isotopic and chemical intra-shell variations in low-Mg calcite of rudist bivalves (Mollusca-Hippuritacea): disequilibrium
1177   fractionations and late Cretaceous seasonality, International Journal of Earth Sciences, 88(3), 551–570, 1999.
1178   Steuber, T., Rauch, M., Masse, J.-P., Graaf, J. and Malkoč, M.: Low-latitude seasonality of Cretaceous temperatures in warm and
1179   cold episodes, Nature, 437(7063), 1341–1344, 2005.
1180   Strahl, J., Philipp, E., Brey, T., Broeg, K. and Abele, D.: Physiological aging in the Icelandic population of the ocean quahog Arctica
1181   islandica, Aquatic Biology, 1(1), 77–83, 2007.
1182   Surge, D. and Lohmann, K. C.: Evaluating Mg/Ca ratios as a temperature proxy in the estuarine oyster, Crassostrea virginica,
1183   Journal of Geophysical Research: Biogeosciences, 113(G2) [online] Available from:
1184   http://onlinelibrary.wiley.com/doi/10.1029/2007JG000623/full (Accessed 28 November 2016), 2008.
1185   Surge, D., Lohmann, K. C. and Dettman, D. L.: Controls on isotopic chemistry of the American oyster, Crassostrea virginica:
1186   implications for growth patterns, Palaeogeography, Palaeoclimatology, Palaeoecology, 172(3), 283–296, 2001.
1187   Surge, D. M., Lohmann, K. C. and Goodfriend, G. A.: Reconstructing estuarine conditions: oyster shells as recorders of
1188   environmental change, Southwest Florida, Estuarine, Coastal and Shelf Science, 57(5), 737–756, doi:10.1016/S0272-
1189   7714(02)00370-0, 2003.
1190   Surlyk, F. and Christensen, W. K.: Epifaunal zonation on an Upper Cretaceous rocky coast, Geology, 2(11), 529–534, 1974.
1191   Surlyk, F. and Sørensen, A. M.: An early Campanian rocky shore at Ivö Klack, southern Sweden, Cretaceous Research, 31(6), 567–
1192   576, 2010.

1193   Tagliavento, M., John, C. M. and Stemmerik, L.: Tropical temperature in the Maastrichtian Danish Basin: Data from coccolith Δ47
1194   and δ18O, Geology, 47(11), 1074–1078, 2019.
1195   Thibault, N., Husson, D., Harlou, R., Gardin, S., Galbrun, B., Huret, E. and Minoletti, F.: Astronomical calibration of upper
1196   Campanian–Maastrichtian carbon isotope events and calcareous plankton biostratigraphy in the Indian Ocean (ODP Hole
1197   762C): Implication for the age of the Campanian–Maastrichtian boundary, Palaeogeography, Palaeoclimatology, Palaeoecology,
1198   337–338, 52–71, doi:10.1016/j.palaeo.2012.03.027, 2012.
1199   Thibault, N., Harlou, R., Schovsbo, N. H., Stemmerik, L. and Surlyk, F.: Late Cretaceous (late Campanian–Maastrichtian) sea-
1200   surface temperature record of the Boreal Chalk Sea, Climate of the Past, 12(2), 429–438, 2016.
1201   Uchikawa, J. and Zeebe, R. E.: The effect of carbonic anhydrase on the kinetics and equilibrium of the oxygen isotope exchange in
1202   the CO2–H2O system: Implications for δ18O vital effects in biogenic carbonates, Geochimica et Cosmochimica Acta, 95, 15–34,
1203   2012.
1204   Ullmann, C. V. and Korte, C.: Diagenetic alteration in low-Mg calcite from macrofossils: a review, Geological Quarterly, 59(1), 3–20,
1205   2015.
1206   Ullmann, C. V., Wiechert, U. and Korte, C.: Oxygen isotope fluctuations in a modern North Sea oyster (Crassostrea gigas)
1207   compared with annual variations in seawater temperature: Implications for palaeoclimate studies, Chemical Geology, 277(1),
1208   160–166, 2010.
1209   Ullmann, C. V., Böhm, F., Rickaby, R. E., Wiechert, U. and Korte, C.: The Giant Pacific Oyster (Crassostrea gigas) as a modern
1210   analog for fossil ostreoids: isotopic (Ca, O, C) and elemental (Mg/Ca, Sr/Ca, Mn/Ca) proxies, Geochemistry, Geophysics,
1211   Geosystems, 14(10), 4109–4120, 2013.
1212   Upchurch Jr, G. R., Kiehl, J., Shields, C., Scherer, J. and Scotese, C.: Latitudinal temperature gradients and high-latitude
1213   temperatures during the latest Cretaceous: Congruence of geologic data and climate models, Geology, 43(8), 683–686, 2015.
1214   Vansteenberge, S., de Winter, N. J., Sinnesael, M., Xueqin, Z., Verheyden, S. and Claeys, P.: Benchtop µXRF as a tool for
1215   speleothem trace elemental analysis: Validation, limitations and application on an Eemian to early Weichselian (125–97 ka)
1216   stalagmite from Belgium, Palaeogeography, Palaeoclimatology, Palaeoecology, 538, 109460,
1217   doi:10.1016/j.palaeo.2019.109460, 2020.
1218   Veizer, J.: Chemical diagenesis of carbonates: theory and application of trace element technique, [online] Available from:
1219   http://archives.datapages.com/data/sepm_sp/SC10/Chemical_Diagenesis.htm, 1983.
1220   Veizer, J. and Prokoph, A.: Temperatures and oxygen isotopic composition of Phanerozoic oceans, Earth-Science Reviews, 146,
1221   92–104, 2015.
1222   Voigt, S. and Schönfeld, J.: Cyclostratigraphy of the reference section for the Cretaceous white chalk of northern Germany,
1223   Lägerdorf–Kronsmoor: A late Campanian–early Maastrichtian orbital time scale, Palaeogeography, Palaeoclimatology,
1224   Palaeoecology, 287(1), 67–80, doi:10.1016/j.palaeo.2010.01.017, 2010.
1225   Voigt, S., Friedrich, O., Norris, R. D. and Schönfeld, J.: Campanian–Maastrichtian carbon isotope stratigraphy: shelf-ocean
1226   correlation between the European shelf sea and the tropical Pacific Ocean, Newsletters on Stratigraphy, 44(1), 57–72, 2010.
1227   Von Bertalanffy, L.: Quantitative laws in metabolism and growth, The quarterly review of biology, 32(3), 217–231, 1957.
1228   Wagreich, M., Hohenegger, J. and Neuhuber, S.: Nannofossil biostratigraphy, strontium and carbon isotope stratigraphy,
1229   cyclostratigraphy and an astronomically calibrated duration of the Late Campanian Radotruncana calcarata Zone, Cretaceous
1230   Research, 38, 80–96, 2012.
1231   Waniek, J. J.: The role of physical forcing in initiation of spring blooms in the northeast Atlantic, Journal of Marine Systems, 39(1–2),
1232   57–82, 2003.
1233   Warter, V., Erez, J. and Müller, W.: Environmental and physiological controls on daily trace element incorporation in Tridacna crocea
1234   from combined laboratory culturing and ultra-high resolution LA-ICP-MS analysis, Palaeogeography, Palaeoclimatology,
1235   Palaeoecology, 496, 32–47, doi:10.1016/j.palaeo.2017.12.038, 2018.
1236   Watanabe, T., Suzuki, A., Kawahata, H., Kan, H. and Ogawa, S.: A 60-year isotopic record from a mid-Holocene fossil giant clam
1237   (Tridacna gigas) in the Ryukyu Islands: physiological and paleoclimatic implications, Palaeogeography, Palaeoclimatology,
1238   Palaeoecology, 212(3–4), 343–354, 2004.
1239   Weiner, S. and Dove, P. M.: An overview of biomineralization processes and the problem of the vital effect, Reviews in mineralogy
1240   and geochemistry, 54(1), 1–29, 2003.
1241   Weis, D., Kieffer, B., Maerschalk, C., Barling, J., Jong, J. de, Williams, G. A., Hanano, D., Pretorius, W., Mattielli, N., Scoates, J. S.,
1242   Goolaerts, A., Friedman, R. M. and Mahoney, J. B.: High-precision isotopic characterization of USGS reference materials by
1243   TIMS and MC-ICP-MS, Geochemistry, Geophysics, Geosystems, 7(8), Q08006, doi:10.1029/2006GC001283, 2006.
1244   Wendler, I.: A critical evaluation of carbon isotope stratigraphy and biostratigraphic implications for Late Cretaceous global
1245   correlation, Earth-Science Reviews, 126, 116–146, doi:10.1016/j.earscirev.2013.08.003, 2013.
1246   de Winter, N. J. and Claeys, P.: Micro X-ray fluorescence (µXRF) line scanning on Cretaceous rudist bivalves: A new method for
1247   reproducible trace element profiles in bivalve calcite, edited by M. R. Petrizzo, Sedimentology, 64(1), 231–251,
1248   doi:10.1111/sed.12299, 2016.
1249   de Winter, N. J., Sinnesael, M., Makarona, C., Vansteenberge, S. and Claeys, P.: Trace element analyses of carbonates using
1250   portable and micro-X-ray fluorescence: performance and optimization of measurement parameters and strategies, Journal of
1251   Analytical Atomic Spectrometry, 32(6), 1211–1223, 2017b.
1252   de Winter, N. J., Goderis, S., Dehairs, F., Jagt, J. W., Fraaije, R. H., Van Malderen, S. J., Vanhaecke, F. and Claeys, P.: Tropical
1253   seasonality in the late Campanian (late Cretaceous): Comparison between multiproxy records from three bivalve taxa from
1254   Oman, Palaeogeography, Palaeoclimatology, Palaeoecology, 485, 740–760, 2017a.
1255   de Winter, N. J., Vellekoop, J., Vorselmans, R., Golreihan, A., Soete, J., Petersen, S. V., Meyer, K. W., Casadio, S., Speijer, R. P.
1256   and Claeys, P.: An assessment of latest Cretaceous Pycnodonte vesicularis (Lamarck, 1806) shells as records for
1257   palaeoseasonality: a multi-proxy investigation, Climate of the Past, 14(6), 725–749, 2018.
1258   de Winter, N. J., Goderis, S., Malderen, S. J. M. V., Sinnesael, M., Vansteenberge, S., Snoeck, C., Belza, J., Vanhaecke, F. and
1259   Claeys, P.: Subdaily-Scale Chemical Variability in a Torreites Sanchezi Rudist Shell: Implications for Rudist Paleobiology and
1260   the Cretaceous Day-Night Cycle, Paleoceanography and Paleoclimatology, 35(2), e2019PA003723,
1261   doi:10.1029/2019PA003723, 2020a.

1262 de Winter, N. J., Vellekoop, J., Clark, A. J., Stassen, P., Speijer, R. P. and Claeys, P.: The giant marine gastropod Campanile
1263   giganteum (Lamarck, 1804) as a high-resolution archive of seasonality in the Eocene greenhouse world, Geochemistry,
1264   Geophysics, Geosystems, n/a(n/a), e2019GC008794, doi:10.1029/2019GC008794, 2020b.
1265 Yang, D., Huang, Y., Guo, W., Huang, Q., Ren, Y. and Wang, C.: Late Santonian-early Campanian lake-level fluctuations in the
1266   Songliao Basin, NE China and their relationship to coeval eustatic changes, Cretaceous Research, 92, 138–149,
1267   doi:10.1016/j.cretres.2018.07.008, 2018.
1268 Yoshimura, T., Tanimizu, M., Inoue, M., Suzuki, A., Iwasaki, N. and Kawahata, H.: Mg isotope fractionation in biogenic carbonates
1269   of deep-sea coral, benthic foraminifera, and hermatypic coral, Anal Bioanal Chem, 401(9), 2755, doi:10.1007/s00216-011-5264-
1270   0, 2011.
1271 Zimmt, J. B., Lockwood, R., Andrus, C. F. T. and Herbert, G. S.: Sclerochronological basis for growth band counting: A reliable
1272   technique for life-span determination of Crassostrea virginica from the mid-Atlantic United States, Palaeogeography,
1273   Palaeoclimatology, Palaeoecology, 516, 54–63, 2018.
1274